

High-Angle Normal Faulting at the Tangra Yumco Graben (Southern Tibet) since ~15 Ma

Reinhard Wolff,^{1,*} Ralf Hetzel,¹ István Dunkl,² Qiang Xu,³ Michael Bröcker,⁴
and Aneta A. Anczkiewicz⁵

1. Institut für Geologie und Paläontologie, Westfälische Wilhelms-Universität Münster, Corrensstraße 24, 48149 Münster, Germany; 2. Institut für Sedimentologie und Umweltgeologie, Universität Göttingen, Goldschmidtstraße 3, 37077 Göttingen, Germany; 3. Institute of Tibetan Plateau Research, Chinese Academy of Sciences, Lincui Road, Chaoyang District, Beijing 100101, China; 4. Institut für Mineralogie, Westfälische Wilhelms-Universität Münster, Corrensstraße 24, 48149 Münster, Germany; 5. Institute of Geological Sciences, Polish Academy of Sciences, Senacka 1, 31-002 Kraków, Poland

ABSTRACT

Several active graben systems in Tibet and the Himalaya are the expression of ongoing east-west extension, but the significance and history of normal faulting in this large region are still debated. Here, we present geo- and thermo-chronological data for a granite intrusion in the footwall of an active high-angle normal fault at the Tangra Yumco graben to constrain the onset and history of normal faulting. Crystallization of the granitic rocks occurred at 87 ± 1 Ma, as revealed by U/Pb zircon dating. After an initial phase of rapid cooling from magmatic temperatures, a later phase of slow cooling is recorded by Rb/Sr biotite ages between ~72 and ~60 Ma. The elevation dependence of the Rb/Sr ages suggests that cooling was controlled by erosion, which proceeded at a rate of ~0.05 km/My during the latest Cretaceous and early Paleocene. The subsequent history of normal faulting is recorded by zircon (U-Th)/He ages of 12.5 ± 1.1 and 9.7 ± 0.7 Ma, apatite fission-track ages between 10.8 ± 1.7 and 7.8 ± 1.2 Ma, and apatite (U-Th)/He ages from 4.9 ± 0.4 to 3.0 ± 0.2 Ma. Thermokinematic modeling of these age data indicates that normal faulting started at 14.5 ± 1.8 Ma at a rate of ~0.3 km/My and accelerated to ~0.7 km/My in the Pliocene. Our age constraint for the initiation of faulting supports a widespread onset of rifting in Tibet at ~15–10 Ma, as reported for other graben systems. Finally, we suggest that the distribution of high-angle and low-angle normal faults is controlled by their position relative to the India-Asia convergence vector and by lateral variations in the thermal state of the lithosphere.

Online enhancements: supplemental table, appendix figure.

Introduction

The Tibetan-Himalayan orogen is the result of the ongoing continent-continent collision between India and Asia, which started in the early Cenozoic (e.g., Molnar and Tapponnier 1975; Rowley 1996; Yin and Harrison 2000; Zhu et al. 2005; Zhang et al. 2012; DeCelles et al. 2014). At a late stage of this long-lasting convergence history, the formation of a series of graben systems and conjugate strike-slip faults led to a significant amount of E-W extension, while the Himalayan thrust belt has continuously

accommodated arc-normal shortening (Molnar and Tapponnier 1978; Armijo et al. 1986; Harrison et al. 1992; Taylor et al. 2003; P. Kapp et al. 2008; Styron et al. 2011; Ratschbacher et al. 2011). The extensional structures occur not only in southern and central Tibet (i.e., the Lhasa and Qiangtang terranes) but also south of the Indus-Tsangpo suture zone in the Himalayan mountain chain, where they record arc-parallel extension of the High Himalaya (e.g., Styron et al. 2011). The strike directions of many graben-bounding normal faults define a diverging pattern with a symmetry axis at ~87°E, which is oriented sub-parallel to the India-Asia convergence direction, suggesting that the stress field generated by the conti-

Manuscript received November 30, 2017; accepted August 17, 2018; electronically published November 7, 2018.

* Author for correspondence; email: rwolff@uni-muenster.de.

[The Journal of Geology, 2019, volume 127, p. 15–36] © 2018 by The University of Chicago.
All rights reserved. 0022-1376/2019/12701-0002\$15.00. DOI: 10.1086/700406

mental collision exerts an important control on the orientation of the graben systems (Kapp and Guynn 2004; fig. 1). East and west of this symmetry axis, India's motion relative to Asia becomes increasingly oblique, which causes an arc-parallel component of extension that increases away from the symmetry axis (Seeber and Pêcher 1998; Styron et al. 2011).

While some graben systems in Tibet and the Himalaya are bounded by high-angle normal faults,

others are dominated by low-angle detachment faults (fig. 1). In general, these two end-member types of crustal extension differ with respect to rates of faulting and total amount of extension as well as in topographic evolution and basin architecture (e.g., Forsyth 1992; Friedmann and Burbank 1995). Parameters that control the structural style and magnitude of extension include the thermal state of the crust and mantle lithosphere, the intracrustal strength con-

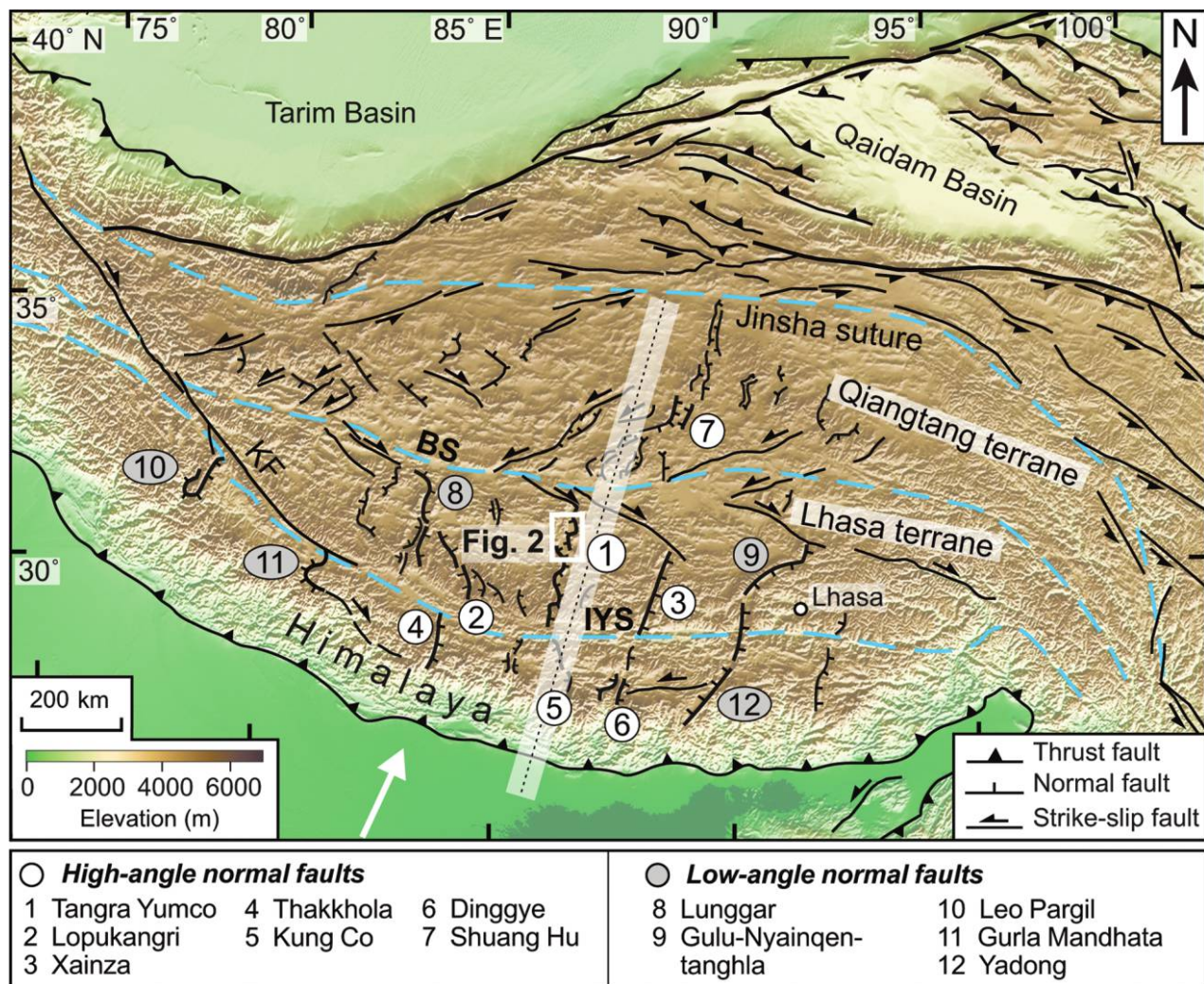


Figure 1. Digital elevation model of the Tibetan Plateau and the Himalaya, showing the location of major rift systems; modified from Armijo et al. (1986, 1989), Taylor et al. (2003), and Rades et al. (2015). The dashed line underlain by white color indicates the symmetry axis of Kapp and Guynn (2004). Rifts with high-angle normal faults are marked by white circles, whereas those dominated by low-angle detachment faults are marked by gray circles. 1 = Tangra Yumco (this study); 2 = Lopukangri (Murphy et al. 2010; Sanchez et al. 2013); 3 = Xainza (Armijo et al. 1986); 4 = Thakkhola (Coleman and Hodges 1995; Garzzone et al. 2003); 5 = Kung Co (Mahéo et al. 2007; Lee et al. 2011); 6 = Dinggye rift (Arma Drime; Jessup et al. 2008; Kali et al. 2010); 7 = Shuang Hu (Blisniuk et al. 2001); 8 = Lunggar (P. Kapp et al. 2008; Styron et al. 2013, 2015; Sundell et al. 2013); 9 = Gulu-Nyainqentanghla (Harrison et al. 1995; J. Kapp et al. 2005; Ratschbacher et al. 2011); 10 = Leo Pargil (Thiede et al. 2006); 11 = Gurla Mandhata (Murphy et al. 2002; McCallister et al. 2014); 12 = Yadong (Ratschbacher et al. 2011). The white arrow indicates the convergence vector of India relative to Asia. Suture zones are shown as dashed blue lines. BS = Bangong suture; IYS = Indus-Yarlung suture; KF = Karakorum fault.

trast between upper and lower crust, and structures inherited from older phases of deformation (e.g., Buck 1993; Wijns et al. 2005; Labrousse et al. 2016). Hence, the occurrence of both high-angle normal faults and detachment faults suggests that the mechanical properties of the crust and mantle lithosphere are spatially variable.

A key piece of information needed to understand the geodynamic significance of the extensional structures within the wider framework of the India-Asia collision zone is the timing of the initiation of normal faulting and the rate of faulting through time. One of the first age estimates for the initiation of extension was given by Molnar et al. (1993), who argued that the convective removal of the mantle lithosphere caused widespread surface uplift and thereby the onset of extension in Tibet at ~ 8 Ma. This age estimate was supported by diffusion modeling of Ar/Ar data on K-feldspar in the normal-fault-bounded mountain range of the Nyainqentanghla Shan shortly thereafter (Harrison et al. 1995). However, an older age of ~ 13 Ma for the regional uplift of Tibet, based on the age of K-rich volcanic rocks derived from the lithospheric mantle, was suggested by Turner et al. (1993), and an even older age of 14.3 ± 0.9 Ma for the onset of normal faulting in Nepal was derived from Ar/Ar dating of fault-related muscovite (Coleman and Hodges 1995). Since these early studies, a significant amount of work has been dedicated to better constraining the history of normal faulting in Tibet and the Himalaya, mainly using low-temperature thermochronology. In combination with thermokinematic modeling, low-temperature thermochronology is a powerful tool to determine the history of faulting in continental rifts and orogenic belts (e.g., Dunkl et al. 1998; Ehlers et al. 2001; Grasemann and Dunkl 2003; Ehlers 2005; Stockli 2005; Campani et al. 2010; Wolff et al. 2012; Styron et al. 2013). So far, most studies that employed this technique in Tibetan rift systems have focused on low-angle normal faults (Harrison et al. 1995; J. Kapp et al. 2005; P. Kapp et al. 2008; Ratschbacher et al. 2011; Styron et al. 2013, 2015; Sundell et al. 2013; McCallister et al. 2014). Thermochronological studies on rifts bounded by high-angle normal faults exist only for the Kung Co graben (Mahéo et al. 2007; Lee et al. 2011), the Thakkhola graben (Coleman and Hodges 1995; Lee et al. 2011), and the Dinggye rift (Jessup et al. 2008; Kali et al. 2010), which are all located south of the Indus-Yarlung suture (fig. 1).

In the Lhasa terrane, detailed geo- and thermochronological studies on the temporal evolution of rifts bounded by high-angle normal faults are still lacking, even though two episodes of faulting, at ~ 13 and ~ 5 Ma, were postulated for the Tangra

Yumco rift (Dewane et al. 2006). Likewise, thermokinematic modeling, which allows us to take heat advection during footwall uplift and erosion into account, has also not been employed on high-angle normal faults in the Lhasa terrane. Here, we present U/Pb zircon and Rb/Sr biotite ages as well as low-temperature thermochronological data for the footwall of a high-angle normal fault at the Tangra Yumco rift (fig. 1). Apatite and zircon (U-Th)/He (AHe and ZHe, respectively) ages, together with apatite fission-track (AFT) ages, allow us to reconstruct the history of normal faulting and rock exhumation by thermokinematic modeling. Our results, together with published geological, geochronological, and geophysical data, indicate that the style and rate of normal faulting in southern Tibet are spatially variable. We suggest that these variations are controlled by—among other factors—the position of the rift systems within the collision zone and the thermal state of the lower crust in the vicinity of the extensional structures.

Geological Setting of the Tangra Yumco Graben

The 250-km-long Tangra Yumco rift system extends from the Indus-Yarlung suture in the south to a dextral strike-slip fault near the Bangong suture in the north (Armijo et al. 1986; Taylor et al. 2003) and follows almost exactly the symmetry axis proposed by Kapp and Guynn (2004; fig. 1). Our study area is located in the northern part of the rift system, where one of the largest lakes in Tibet, Tangra Yumco, is situated in the Tangra Yumco graben (fig. 2a). The two most prominent normal faults of the graben trend NW-SE and occur at the northern and southern shores of this lake (fig. 2b). The linear trace of both faults in map view and well-developed triangular facets in their footwalls (fig. 3a) indicates that these structures are tectonically active high-angle normal faults. In this study, we focus on the 30-km-long normal fault at the southern shore of Tangra Yumco. The mountain range in the fault footwall is characterized by well-developed U-shaped valleys (fig. 3a). The highest parts of the range, which rises to 6382 m above sea level, are covered by snow fields and small glaciers.

The bedrock exposed in the studied mountain range comprises mainly undeformed to weakly deformed granitoid rocks, which are well suited for applying geochronological methods (fig. 3b). In general, such granitoid intrusions in the northern Lhasa terrane are Early Cretaceous in age, with U/Pb ages between 140 and 100 Ma (Xu et al. 1985; Kapp et al. 2007; Hetzel et al. 2011; Haider et al. 2013). In contrast, the intrusive rocks in the footwall of the studied normal

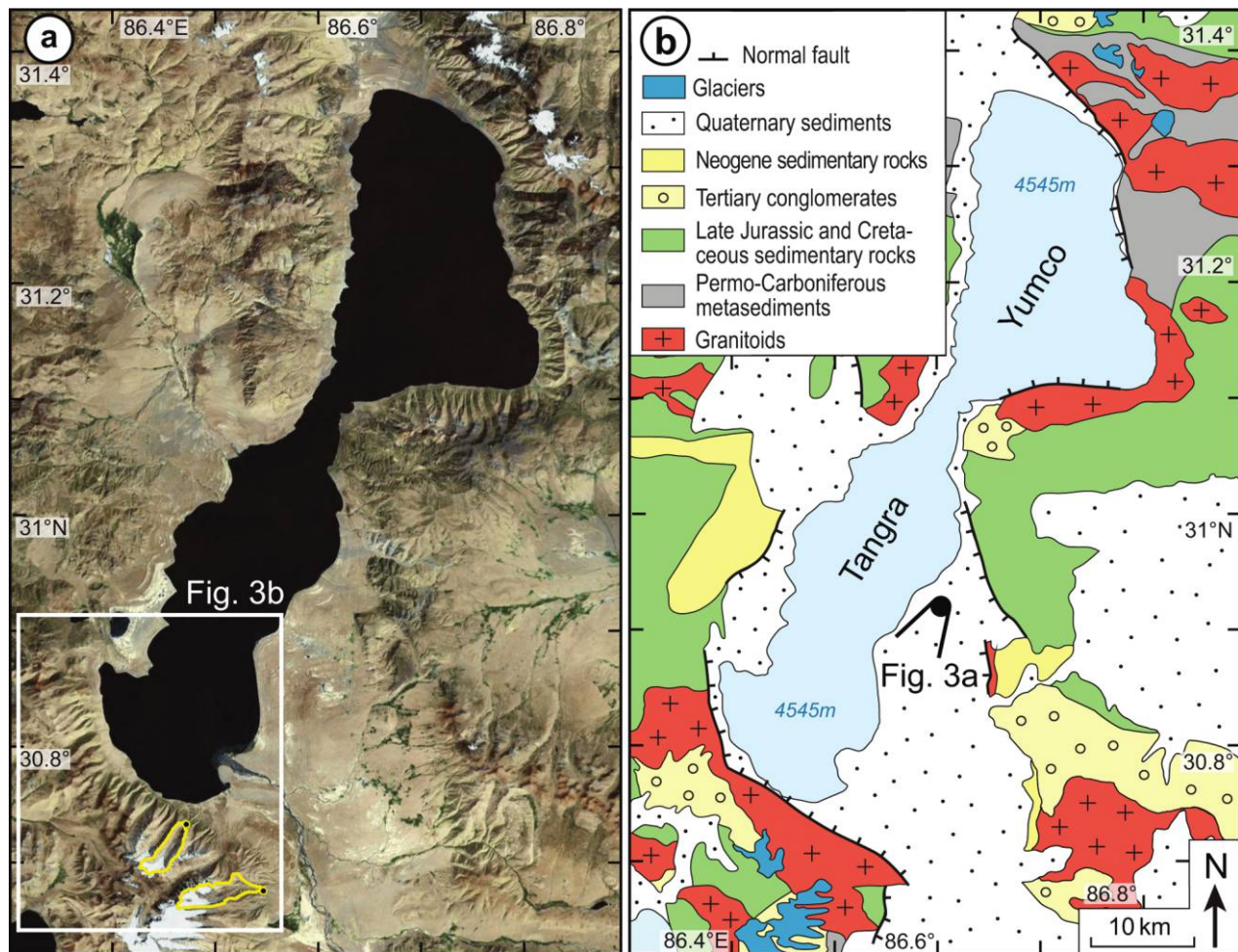


Figure 2. *a*, Satellite image of the Tangra Yumco region, from Google Earth (white rectangle depicts area shown in fig. 3*b*). The positions of two stream-sediment samples and their catchments are shown by black points and yellow lines (after Rades et al. 2015). *b*, Simplified geological map of the Tangra Yumco region, with the location of active normal faults. The map is based on the 1:250,000 geological maps of the Bangduo and Cuomai districts (Geological Survey of Jiangxi Province 2002). The black circle indicates the site where the photograph shown in figure 3*a* was taken.

fault were interpreted as Eocene in age on the basis of a K-Ar age of 46.5 ± 0.9 Ma obtained in the western part of the study area (fig. 3*b*; Geological Survey of Jiangxi Province 2002 and related 1:250,000 geological map). We show below that this age dates merely the cooling of the granitic rocks but not their intrusion. Apart from the intrusive rocks, Mesozoic sedimentary rocks and Tertiary conglomerates are exposed in the mountain range southwest of Tangra Yumco (Geological Survey of Jiangxi Province 2002).

Sampling and Analytical Methods

To constrain the crystallization age and subsequent cooling history of the granitoid rocks in the mountain range southwest of Tangra Yumco, we em-

ployed U/Pb dating on zircon, Rb/Sr dating on biotite, and ZHe and AHe dating, as well as AFT dating. Three samples of biotite-bearing granite were collected from bedrock outcrops at elevations of 4802, 5100, and 5370 m (fig. 3*a*) and at horizontal distances from the trace of the normal fault of 0.4, 1.0, and 2.1 km, respectively (fig. 3*b*). Sampling at higher elevations was prohibited by bad weather conditions and the high altitude of the study area. Investigations of thin sections did not provide any evidence for petrological differences between the three samples or any signs of a retrograde or hydrothermal alteration. In particular, brown biotite is not chloritized, and K-feldspar shows no signs of sericitization. As we show below, the U/Pb ages for the highest and lowest samples are identical within errors,

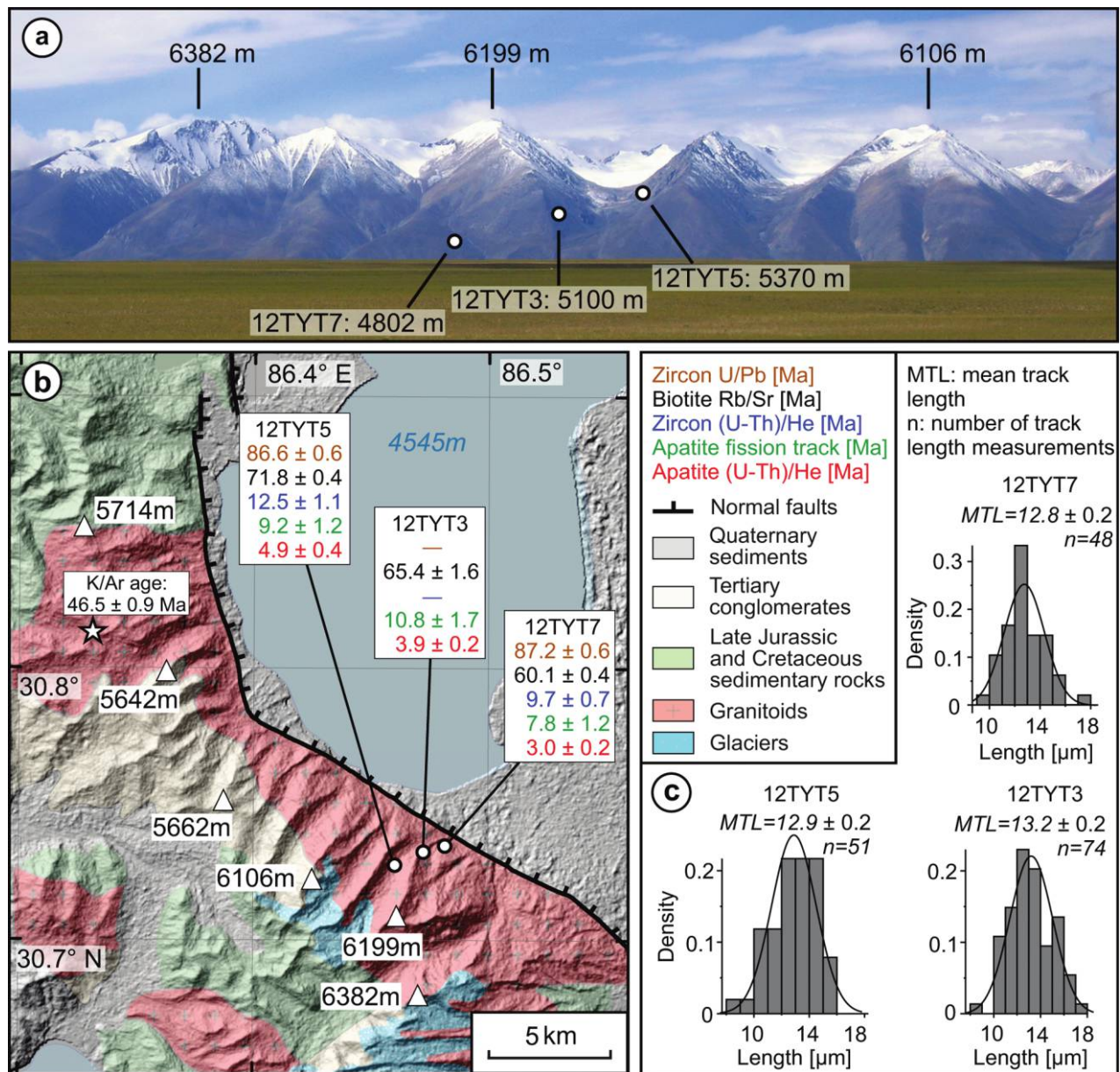


Figure 3. *a*, Frontal view of the mountain range in the footwall of the studied normal fault with the position of the three samples. Note the triangular facets in the lower part of the range and the well-developed U-shaped valleys. Note that these valleys are not hanging valleys. Photograph taken toward the south-southwest from the position indicated by the black circle in figure 2*b*. *b*, Geological map with sample locations and geochronological results. *c*, Central ages and confined track length distributions of the apatite fission-track samples. The track length distributions are unimodal, and the mean track lengths (MTLs) are between 12.8 and 13.2 μm (n = number of measured confined fission tracks).

indicating that the samples belong to a single granite intrusion. In the following, we describe the analytical procedures of the different dating techniques.

In situ U/Pb dating was performed by laser-ablation single-collector sector-field inductively coupled plasma mass spectrometry (LA-SF-ICP-MS; Frei and Gerdes 2009). A Thermo Finnigan Element 2 mass spectrometer coupled to a Resonetics Ex-

cimer laser ablation system was used. All age data were obtained by single-spot analyses with a laser beam diameter of $\sim 33 \mu\text{m}$ and a crater depth of $\sim 10 \mu\text{m}$. The laser was fired at a repetition rate of 5 Hz and at nominal laser energy output of 25%. Two laser pulses were used for preablation. Analytes of ^{238}U , ^{235}U , ^{232}Th , ^{208}Pb , ^{207}Pb , ^{206}Pb , ^{204}Pb , and ^{202}Hg were measured by ICP-MS. The data reduc-

tion is based on the processing of ~50 selected time slices (corresponding to ~14 s), starting ~3 s after the beginning of the signal. The age calculation and quality control are based on the drift and fractionation correction by standard-sample bracketing using GJ-1 zircon reference material (Jackson et al. 2004). For further control, the Plešovice zircon (Sláma et al. 2008) and the 91500 zircon (Wiedenbeck et al. 1995) were analyzed as secondary standards. The age results of the standards were consistently within 2σ of the published isotope dilution (ID) TIMS values. Drift and fractionation corrections and data reductions were performed with the software UranOS (Dunkl et al. 2008). The concordia plots and age spectra were constructed with Isoplot/Ex 3.0 (Ludwig 2012). The dated zircon crystals have a significantly lower radiation-damage density (calculated from their U and Th concentrations and the respective decay schemes, following Sliwinski et al. 2017) than the zircon reference materials used for correction of the fractionation (5×10^{16} in the samples vs. 6.1×10^{17} , 7.4×10^{17} , and 3.1×10^{17} alpha decay events/g, respectively, in the GJ-1, Plešovice, and 91500 zircon standards). As the radiation-damage density influences the ablation rate of zircons (Marillo-Sialer et al. 2014), it has to be corrected for, which was done following Sliwinski et al. (2017), who investigated this effect using 22 different zircon reference materials with a wide range of damage densities. The radiation-damage-corrected ages are between 0.9 and 2.2 Ma older than the uncorrected ones and can be considered the most reliable approximation of the crystallization age of the zircons (table S1, available online).

Rb/Sr TIMS analysis was carried out at the Institut für Mineralogie, Universität Münster. Before dissolution, handpicked biotite and apatite mineral concentrates (>99% pure) were repeatedly rinsed in ultrapure water and ethanol. Mineral separates were mixed with an ^{87}Rb - ^{84}Sr spike in Teflon vials and dissolved in HF-HNO₃ (5:1) on a hot plate overnight. After complete evaporation, 6 N HCl was added to the residue. This mixture was again homogenized on a hot plate overnight. After a second evaporation to dryness, Rb and Sr were separated by standard ion-exchange procedures (AG 50W-X8 resin) on quartz glass columns, with 2.5 N HCl as eluent. For mass-spectrometric analysis, Rb was loaded with H₂O on Ta filaments; Sr was loaded with TaF₅ on W filaments. All samples were measured in static mode with a VG Sector 54 TIMS (Rb) and a Thermo Finnigan Triton TIMS (Sr). The analyses were carried out in two sessions with external reproducibilities (2σ) of National Bureau of Standards (NBS) standard 987 of 0.710278 ± 0.000010

($n = 14$) and 0.710289 ± 0.000010 ($n = 9$). Total procedural blanks were <20 pg for Rb and <30 pg for Sr. Correction for mass fractionation is based on $^{86}\text{Sr}/^{88}\text{Sr} = 0.1194$. For correction of Rb ratios, a factor deduced from multiple measurements of NBS standard 607 was used. All ages and elemental concentrations were calculated by means of Isoplot/Ex 4.15 (Ludwig 2012), using the ^{87}Rb decay constant recommended by Villa et al. (2015). For isochron calculations, $^{87}\text{Rb}/^{86}\text{Sr}$ and $^{87}\text{Sr}/^{86}\text{Sr}$ ratios were assigned 2σ uncertainties of 1% and 0.005%, respectively. The error on isochron ages indicates the 95% confidence level.

For (U-Th)/He thermochronology, intact and euhedral zircon and apatite crystals without inclusions were handpicked from heavy-liquid separates. The single crystals were wrapped in 1 × 1-mm platinum capsules and degassed in high vacuum by heating with an infrared diode laser at the GÖochron laboratories, University of Göttingen. The extracted gas was purified with a SAES Ti-Zr getter at 450°C and spiked with ^3He . The chemically inert noble gases and a minor amount of other trace gases were then expanded into a Hiden triple-filter quadrupole mass spectrometer equipped with an ion-counting detector. Crystals were checked for complete degassing of helium by sequential reheating and helium measurement. After degassing, crystals were retrieved from the gas extraction line, unpacked, spiked with calibrated ^{230}Th and ^{233}U solutions, and dissolved in pressurized Teflon bombs at 220°C with distilled 48% HF + 65% HNO₃ for 5 d and 4% HNO₃ for 1 d for zircons and apatites, respectively. Spiked solutions were analyzed by the ID method with a Perkin Elmer Elan DRC II and an iCAP Q ICP-MS equipped with an APEX microflow nebulizer. Crystal shape parameters were determined by multiple microphotographs and used to determine correction factors for alpha ejection (Farley et al. 1996) with the constants of Hourigan et al. (2005). The radiation-damage densities of the apatite and zircon crystals range from 1.5×10^{14} to 8.1×10^{14} alpha decay events/g and from 9.0×10^{15} to 2.0×10^{16} alpha decay events/g, respectively, which is well below the threshold for damage-induced decrease of closure temperatures (Flowers et al. 2009; Gautheron et al. 2009; Guenther et al. 2013).

The AFT dating by the external-detector method (Gleadow 1981) was carried out at the Institute of Geological Sciences, Polish Academy of Sciences, in Kraków (Poland). The selected apatite crystals were embedded in epoxy resin and polished in five steps with Al₂O₃ suspensions. Then they were etched in 5 N HNO₃ at a temperature of 21°C for

20 s to reveal spontaneous fission tracks (Zaun and Wagner 1985; Donelick et al. 1999). Neutron irradiation of samples, age standards (Fish Canyon Tuff, Durango apatite, and Mount Dromedary apatite), and a CN5 glass dosimeter was performed at the TRIGA reactor at Oregon State University. After irradiation, the induced fission tracks in the mica detectors were revealed by etching in 40% HF for 45 min. Track counting and length measurements were made with a NIKON Eclipse E-600 microscope computer-controlled stage system (Dumitru 1993) with 1250 \times magnification. Calculations and plots were performed with the software Trackkey (Dunkl 2002). The fission-track ages were determined by the zeta method (Hurford and Green 1983), with age standards listed in Hurford (1998). Error calculation followed the procedure of Green (1981). By measurement of the etch pit diameters (Dpars), the fission-track annealing kinetics was assessed (Burtner et al. 1994).

Geochronological Results

U/Pb dating of zircon from the topographically highest and lowest samples (12TYT5 and 12TYT7) yielded concordant U/Pb ages of 86.6 ± 0.6 and 87.2 ± 0.6 Ma, respectively, which agree within error (fig. 4). The analytical details are contained in table S1. The results of the Rb/Sr analysis are summarized in table 1. The $^{87}\text{Rb}/^{86}\text{Sr}$ ratios of the different biotite grain size fractions from each sample have a significant spread. When combined with the low $^{87}\text{Rb}/^{86}\text{Sr}$ ratios of the apatites, the data from the three samples yield internal mineral isochron ages of 71.8 ± 0.4 , 65.4 ± 1.6 , and 60.6 ± 2.4 Ma (fig. 5). If the biotite fraction $>710 \mu\text{m}$ of sample 12TYT7 is not considered in the age calculation, the resulting isochron age is slightly younger (i.e., 60.1 vs. 60.6 Ma) but has a significantly smaller error (i.e., 60.1 ± 0.4 Ma), and the MSWD value decreases to 2.0. This decrease in the MSWD value may indicate the presence of minor inclusions in the $>710\text{-}\mu\text{m}$ grain size fraction.

The results of the (U-Th)/He thermochronology are presented in table 2. The single-crystal AHe and ZHe ages cluster tightly for all samples (3–7 crystals per sample were analyzed). Note that sample 12TYT3 did not yield zircons of sufficient quality for ZHe dating. The unweighted average ages for the apatite of the three samples are 4.9 ± 0.4 , 3.9 ± 0.2 , and 3.0 ± 0.2 Ma (table 2). The average ZHe ages from samples 12TYT5 and 12TYT7 are 12.5 ± 1.1 and 9.7 ± 0.7 Ma, respectively (table 2). The three AFT samples yielded central ages ranging from 10.8 ± 1.7 to 7.8 ± 1.2 Ma (table 3). All samples passed the χ^2 test and are therefore considered to form one age

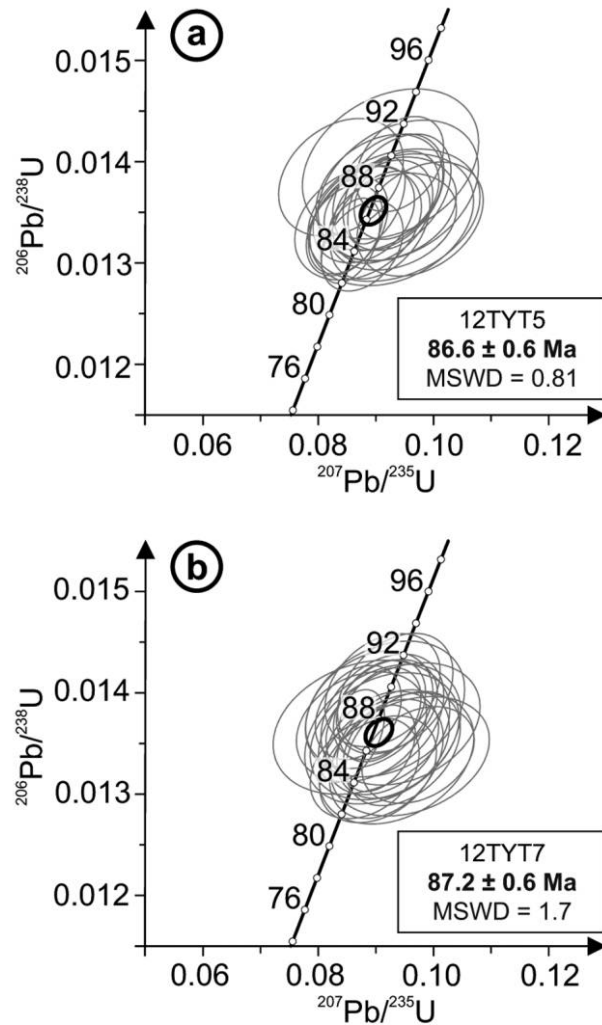


Figure 4. U/Pb concordia diagrams of the two dated zircon samples. The two ages are given with 2σ error.

population. The mean Dpar values are in the narrow range of 2.2–2.3 μm (table 3).

Age-Elevation Relationships

Our age data exhibit positive correlations between age and elevation for each of the three low-temperature thermochronometers, with the exception of one AFT age (fig. 6). This elevation dependence reflects the progressive cooling of the footwall during normal faulting and exhumation. The two ZHe ages indicate that the topographically highest and lowest samples cooled through the closure temperature of $\sim 180^\circ\text{C}$ (Reiners 2005) at about 12.5 and 9.7 Ma, respectively. Therefore, the oldest ZHe age of 12.5 ± 1.1 Ma likely provides a minimum age for the initiation of normal faulting. The AFT ages of ~ 10.8 to ~ 7.8 Ma and the AHe ages of ~ 4.9 to ~ 3.0 Ma in-

Table 1. Sample Locations and Details of the Rb-Sr Analysis

Sample, mineral	Elevation (m)	Latitude (°N)	Longitude (°E)	Grain size (mm)	Rb (ppm)	Sr (ppm)	$^{87}\text{Rb}/^{86}\text{Sr}$	$^{87}\text{Sr}/^{86}\text{Sr} \pm 2\sigma$	Age $\pm 2\sigma$ (Ma)
12TYT5	5370	30.7272	86.4611						71.8 \pm .4
Biotite				>710	756	27	81.86	.792008 \pm .000007	
Biotite				710–500	767	14	165.2	.875826 \pm .000016	
Biotite				500–355	789	12	197.4	.907479 \pm .000009	
Apatite					2.0	294	.0198	.709770 \pm .000006	
12TYT3	5100	30.7326	86.4725						65.4 \pm 1.6
Biotite				>710	667	19	104.0	.806158 \pm .000009	
Biotite				710–500	691	12	165.5	.860573 \pm .000008	
Biotite				500–355	635	19	99.01	.799445 \pm .000006	
Apatite					1.9	321	.0170	.709838 \pm .000005	
Apatite					.8	320	.0074	.709755 \pm .000006	
12TYT7	4802	30.7348	86.4817						60.6 \pm 2.4, 60.1 \pm .4 ^a
Biotite				>710	739	25	84.49	.782962 \pm .000012	
Biotite				710–500	780	18	125.1	.815764 \pm .000013	
Biotite				500–355	797	14	163.1	.846453 \pm .000011	
Apatite					1.8	274	.0191	.710139 \pm .000006	

Note. The $^{87}\text{Rb}/^{86}\text{Sr}$ ratios were assigned an uncertainty of 1% (2σ). For age calculation, $^{87}\text{Sr}/^{86}\text{Sr}$ ratios were assigned an uncertainty of 0.005% (2σ). Error on isochron ages indicates 95% confidence level.

^aThe second age is the isochron age of sample 12TYT7 if the >710- μm biotite fraction is not considered.

dicates further cooling below $\sim 60^\circ\text{C}$. A continuous cooling without stagnation or reheating is corroborated by the unimodal track-length distributions of the apatite samples, which have mean track lengths between 12.8 and 13.2 μm (fig. 3c).

Age-elevation data are commonly used to determine exhumation rates under the assumption of temporarily and spatially invariant horizontal isotherms (Wagner and Reimer 1972). In that case, the slope of the regression line in age-elevation plots can be interpreted as the exhumation rate. With this approach, our AHe and ZHe ages yield exhumation rates of 0.31 ± 0.07 and 0.20 ± 0.09 km/My, respectively (fig. 6). However, the above-mentioned assumption of undisturbed isotherms is unlikely to be met for our data, because normal faulting and footwall erosion lead to heat advection and an increase of the geothermal gradient through time (Stüwe et al. 1994; Mancktelow and Grasemann 1997; Reiners and Ehlers 2005). To take these effects into account and to quantify the history of normal faulting in more detail, we employed thermokinematic modeling, as described in the next section.

Thermokinematic Modeling

For thermokinematic modeling of the age data, we used the code PECUBE, a finite-element code that solves the three-dimensional heat-transport equation and is able to predict the time-dependent thermal evolution of fault-bounded blocks (Braun 2003; Braun et al. 2012). PECUBE uses time-temperature

histories to calculate apparent ages for a range of thermochronometers for samples that have reached the model surface. To compute these ages with PECUBE, we selected the He diffusion model for apatite of Farley (2000). For He diffusion in zircon, we adjusted the diffusion model of Reiners et al. (2004) toward a lower closure temperature based on data by Guenthner et al. (2013) to account for the rather low radiation damage of our zircon samples (9.0×10^{15} to 2.0×10^{16} alpha decay events/g). Therefore, we use a value for D_0/a^2 of 37,800/s and an activation energy E_a of 168 kJ/mol in our PECUBE model. These kinetic parameters are equivalent to a zircon closure temperature of $\sim 170^\circ\text{C}$. For AFT, we chose the annealing model of Ketchum et al. (2005).

Our finite-element model is 17 km long, 13 km wide, and 70 km thick to ensure that the thermal history of the modeled samples is not affected by boundary effects. The value of 70 km is similar to the present thickness of the crust in southern Tibet, as derived with the receiver-function method (Nábělek et al. 2009). For our model, we use a basal temperature of 800°C , a radiogenic heat production of $28^\circ\text{C}/\text{My}$, and a thermal diffusivity of $25 \text{ km}^2/\text{My}$ (table 4). These parameters lead to a preextensional geothermal gradient of $45^\circ\text{C}/\text{km}$ in the upper part of the model (i.e., from the model surface to a depth of $\sim 15 \text{ km}$), which we consider reasonable for a thickened continental crust containing a significant amount of granitic rocks with rather high concentrations of the heat-producing elements U, Th, and K. The fault plane in our model has a dip of 65° ,

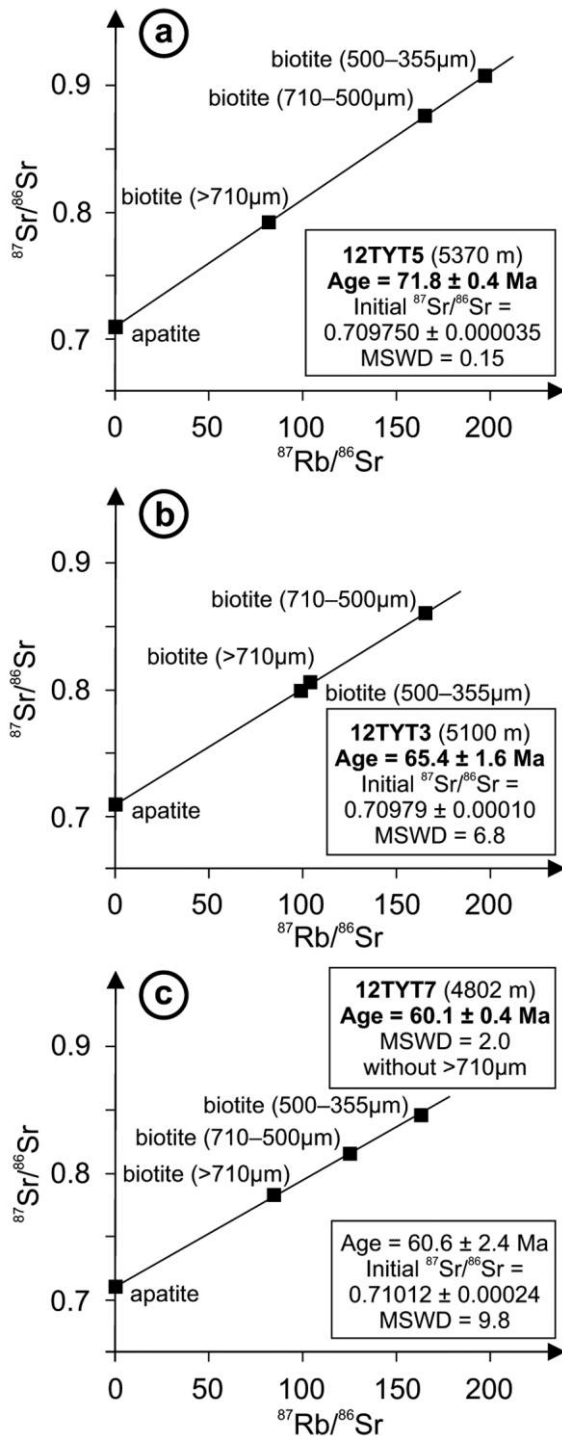


Figure 5. Results of Rb/Sr analysis and the mineral isochron plots for the three samples. The internal isochron ages are given in the boxes. Excluding the biotite fraction $>710\mu\text{m}$ of sample 12TYT7 (c) results in an age of 60.1 ± 0.4 Ma and an MSWD value of 2.0. The error bars are smaller than the symbols.

which changes to 50° above the model surface to account for minor footwall tilting during normal faulting and extension. The topography in our preferred model evolves with time. We start each model at 30 Ma with a flat topography (i.e., zero relief), but from 15 Ma onward the topography evolves linearly to the present-day topography, because the ZHe age of 12.5 ± 1.1 Ma provides a minimum constraint for the onset of faulting. The topography in our PECUBE model has a resolution of ~ 400 m and is derived from a 30-m ASTER (Advanced Spaceborne Thermal Emission and Reflection Radiometer) digital elevation model. We also conducted simulations with a temporally constant present-day topography for comparison with our preferred model.

All model parameters mentioned above (except the topography) remained unchanged during each model run. Using these default values, we attempted to fit the age data by varying only the fault slip rate between different model runs (i.e., from 0.1 to 1.2 km/My) and the time when faulting began. However, with a constant slip rate it is impossible to obtain a reasonable fit to both the ZHe and AHe ages. For example, if modeled and measured ZHe ages did broadly agree (which is the case for, e.g., a slip rate of 0.45 km/My and an onset of normal faulting at 14.5 Ma), the modeled AHe ages are 1.7–2.1 Ma older than the measured ones (table 5). Also, the age differences between the topographically highest and lowest samples are too small for both ZHe and AHe ages (table 5). Note that a rotation of the footwall block during normal faulting would decrease the vertical distance between the samples but cannot also reconcile the young AHe ages with the rather old ZHe ages at a constant rate of faulting. In order to obtain younger AHe ages with the model, fault slip during the final stage of faulting must be faster, whereas a larger spread in the ZHe ages can be obtained only if the initial slip rate is slower than the one used in the constant-slip-rate model. Therefore, we included a change in the rate of faulting in order to better reproduce the age data. As the higher fault slip rate should affect only the AHe ages, the change in the slip rate must occur rather late (e.g., after ~ 5 Ma). We explored different model scenarios in which the slip rate was increased between 5 and 2 Ma. Model runs with a slip-rate increase at 3 Ma yielded the best fit to the ZHe and AHe age data. In models with an earlier or later slip-rate increase, the discrepancy between measured and modeled ages increases.

We now proceed with the determination of the following three model parameters: the time of the onset of normal faulting and the fault slip rates before and after the slip-rate increase at 3 Ma (note that before the onset of normal faulting, no exhumation

Table 2. Results of Apatite and Zircon (U-Th)/He Analysis

Sample, aliquot	Mass of crystal (μg)	Sphere radius (μm)	He			^{238}U			^{232}Th			Sm		Ft ^d	Uncorr. He age (Ma)	Ft-corr. He age $\pm 2\sigma$ (Ma) ^e	Unwtd. avg. age \pm SE (Ma)	
			Vol. (ncc) $\pm 1\sigma$ (%) ^a	Rad. dens. (alpha/g) ^b	Mass (ng) $\pm 1\sigma$ (%)	Conc. (ppm)	Mass (ng) $\pm 1\sigma$ (%)	Conc. (ppm)	Th/U	eU (ppm) ^c	Mass (ng) $\pm 1\sigma$ (%)	Conc. (ppm)						
Apatite (U-Th)/He:																		
12TYT5 (5370 m)																		
1	7	75	.190 \pm 1.5	8.0×10^{14}	.158 \pm 1.9	24.8	.799 \pm 2.4	125.6	5.06	54.4	.758 \pm 8.2	119	.78	4.4	5.7 \pm .5	4.9 \pm .4		
2	11	98	.272 \pm 1.3	7.3×10^{14}	.326 \pm 1.8	32.4	1.249 \pm 2.4	124.2	3.84	61.6	.973 \pm 3.5	97	.84	3.6	4.2 \pm .3			
3	11	76	.268 \pm 1.3	8.1×10^{14}	.302 \pm 1.8	34.1	1.275 \pm 2.4	143.9	4.22	67.9	1.075 \pm 3.5	121	.78	3.6	4.6 \pm .4	3.9 \pm .2		
12TYT3 (5100 m)																		
1	16	105	.335 \pm 1.3	8.1×10^{14}	.276 \pm 1.8	24.9	1.519 \pm 2.4	137.2	5.51	57.1	1.562 \pm 3.2	141	.84	4.3	5.1 \pm .3			
2	9	80	.114 \pm 1.9	4.3×10^{14}	.195 \pm 1.8	27.7	.673 \pm 2.4	95.5	3.45	50.1	.349 \pm 4.6	50	.80	2.6	3.3 \pm .3			
3	10	79	.246 \pm 1.3	5.7×10^{14}	.356 \pm 1.8	30.4	1.330 \pm 2.4	113.6	3.74	57.1	.726 \pm 4.0	62	.79	3.0	3.8 \pm .3			
4	30	89	.170 \pm 1.8	1.5×10^{14}	.235 \pm 2.0	7.8	1.098 \pm 2.4	36.7	4.67	424.0	.883 \pm 3.3	29	.85	2.8	3.3 \pm .2			
5	17	82	.195 \pm 1.8	3.0×10^{14}	.236 \pm 2.0	13.6	.946 \pm 2.4	54.5	4.02	345.7	.736 \pm 3.7	42	.84	3.5	4.1 \pm .3			
6	19	74	.140 \pm 2.0	2.0×10^{14}	.175 \pm 2.2	9.3	.829 \pm 2.4	44.0	4.74	317.1	.644 \pm 3.5	34	.82	3.1	3.7 \pm .3			
7	25	87	.269 \pm 1.7	2.9×10^{14}	.326 \pm 1.9	13.2	1.287 \pm 2.4	52.0	3.95	516.7	.745 \pm 3.6	30	.85	3.5	4.1 \pm .3	3.0 \pm .2		
12TYT7 (4802 m)																		
1	8	71	.164 \pm 1.6	5.3×10^{14}	.318 \pm 1.8	38.1	.934 \pm 2.4	111.8	2.93	64.4	.801 \pm 8.3	96	.77	2.5	3.2 \pm .3			
2	7	79	.101 \pm 2.0	4.2×10^{14}	.162 \pm 1.9	25.0	.651 \pm 2.4	100.7	4.02	48.7	.490 \pm 8.5	76	.79	2.6	3.3 \pm .3			
3	10	81	.117 \pm 1.8	3.6×10^{14}	.279 \pm 1.8	31.9	.798 \pm 2.4	91.3	2.86	53.4	.752 \pm 8.3	86	.80	2.1	2.6 \pm .2			
Zircon (U-Th)/He:																		
12TYT5 (5370 m)																		
1	22	94	6.009 \pm .9	1.1×10^{16}	4.422 \pm 1.8	294.7	3.487 \pm 2.4	232.4	.79	349.3	.050 \pm 14.4	3	.86	9.5	11.0 \pm .6	12.5 \pm 1.1		
2	9	63	5.078 \pm .9	2.0×10^{16}	2.818 \pm 1.8	414.7	6.768 \pm 2.4	995.9	2.40	648.8	.055 \pm 15.7	8	.80	9.5	11.9 \pm .8			
3	24	85	10.529 \pm .9	1.6×10^{16}	6.061 \pm 1.8	345.0	3.953 \pm 2.4	225.0	.65	397.8	.063 \pm 14.7	4	.85	12.5	14.6 \pm .8			
12TYT7 (4802 m)																		
1	2	42	1.104 \pm 1.1	1.7×10^{16}	1.034 \pm 1.8	586.2	1.006 \pm 2.4	570.2	.97	720.2	.007 \pm 37.9	4	.71	7.2	10.1 \pm 1.0			
2	4	62	1.137 \pm 1.0	9.0×10^{15}	1.199 \pm 1.8	351.3	.886 \pm 2.4	259.6	.74	412.3	.006 \pm 42.3	2	.80	6.7	8.4 \pm .6			
3	4	48	1.385 \pm 1.0	1.0×10^{16}	1.206 \pm 1.8	334.9	.997 \pm 2.4	276.9	.83	400.0	.015 \pm 24.2	4	.74	8.0	10.7 \pm .9	9.7 \pm .7		

Note. Vol. = volume; Rad. dens. = radiation-damage density; Conc. = concentration; Uncorr. = uncorrected; corr. = corrected; Unwtd. avg. = unweighted average.

^aUnit of measure is nano-cc (ncc; 10^{-9} cm^3) at standard temperature and pressure.

^bUnit of measure is alpha decay events per gram.

^cEffective uranium content: eU = U (ppm) + 0.253 \times Th (ppm).

^dCorrection factor for alpha ejection (according to Farley et al. 1996).

^eUncertainty of the single-grain age is given with 2σ error. The error includes both the analytical uncertainty and the estimated uncertainty of the ejection correction.

Table 3. Results of Apatite Fission-Track Analysis

Sample	Elevation (m)	No. of crystals	Spontaneous		Induced		Dosimeter ^a		Central age $\pm 1\sigma$ (Ma) ^b	MTL (μm)	No. of measured TL	Dpar (μm)	U (ppm)
			P	N	ρ	N	ρ	N					
12TYT5	5370	20	.09	65	2.01	1375	1.12	3354	9.2 \pm 1.2	12.9 \pm .2	51	2.2 \pm 1.6	23
12TYT3	5100	20	.09	42	1.59	753	1.12	3358	10.8 \pm 1.7	13.2 \pm .2	74	2.2 \pm 1.2	18
12TYT7	4802	20	.10	45	2.48	1118	1.12	3349	7.8 \pm 1.2	12.8 \pm .2	48	2.3 \pm 1.9	27

Note. A ζ value of $348.2 \pm 6.5 \text{ y/cm}^2$ is used. ρ = track densities measured as 10^6 tracks/cm²; N = number of tracks counted; $P(\chi^2)$ = probability of obtaining a χ^2 value for n degrees of freedom (n = no. crystals - 1); MTL = mean track length. Dpar = etch pit diameter.

^aUsing dosimeter glass CN5.

^bCentral age was calculated according to Galbraith and Laslett (1993).

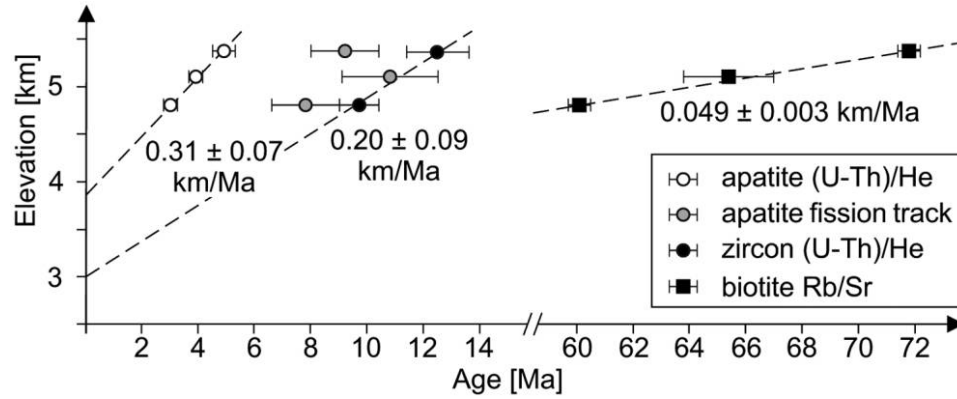


Figure 6. Age-elevation plot with all age data. Under the assumption of temporarily and spatially invariant isotherms, the slopes of the regression lines can be interpreted as exhumation rates. This assumption is unlikely to be met for the low-temperature thermochronologic ages. See text for further details.

occurs in the model). To allow an efficient exploration of a sufficiently wide parameter space, we used a two-step neighborhood algorithm inversion (Sambridge 1999a, 1999b). We chose a time range of 20–3 Ma for the initiation of normal faulting and slip rates of 0.1–1.0 and 0.1–1.2 km/My before and after 3 Ma, respectively. This parameter space was sampled iteratively by PECUBE to minimize the misfit between observed and predicted data. The inversion procedure is controlled by the number of iterations, the number of models calculated for each iteration, and the resampling ratio (cf. Glotzbach et al. 2011). We performed 102 iterations with 99 models for each iteration (i.e., a total of 10,098 models). To ensure a sufficiently explorative sampling of the parameter space, we used a high resampling ratio of 0.9. The misfit resulting from all models was calculated as

$$\phi = \sum_{i=1}^N \left(\frac{\alpha_{i,\text{model}} - \alpha_{i,\text{data}}}{\sigma_{i,\text{data}}} \right)^2,$$

where N is the number of data points, $\alpha_{i,\text{data}}$ are the observed data, $\alpha_{i,\text{model}}$ are the predicted values, and

$\sigma_{i,\text{data}}$ are the uncertainties of the average (U-Th)/He ages and the AFT ages (tables 2, 3). The results of the inversion procedure are shown in two plots, in which the best-fit model is indicated by a star (fig. 7a, 7b). To derive quantitative constraints for the individual parameters and their uncertainties (fig. 7c), we use marginal probability density functions (cf. Glotzbach et al. 2011). For the initiation of normal faulting, we obtain a value of 14.5 ± 1.8 Ma, whereas the fault slip rates before and after 3 Ma are 0.31 ± 0.02 and 0.78 ± 0.05 km/My, respectively. The vertical components of these slip rates are 0.28 ± 0.02 and 0.71 ± 0.05 km/My, respectively (table 6). The exhumation rate between 14.5 and 3.0 Ma is 0.22–0.25 km/My, whereas after 3 Ma it is 0.64–0.68 km/My (table 6; note that the exhumation rate is slightly different for each sample, because the topography in the preferred model evolves with time). The best-fit model with a one-step increase in slip rate predicts AHe ages that are in much better agreement with our age data than those of the constant-slip-rate model, and the same is true for the two ZHe ages (table 5). The AFT age of 8.2 Ma predicted for the topographically highest sample is consistent with the measured AFT age of

Table 4. Parameters Used for the Thermokinematic Model

Parameter	Value
Model size (km)	17×13
Model thickness (km)	70
Finite-element model node spacing (horizontal, vertical; km)	.42, 2.3
Temperature at base of model (°C)	800
Radiogenic heat production (°C/My)	28
Thermal diffusivity (km ² /My)	25
Crustal density (kg/m ³)	2700
Mantle density (kg/m ³)	3200
Atmospheric lapse rate (°C/km)	6.5
Surface temperature (elevation dependent; °C)	2–11
Fault dip (deg)	65

Table 5. Results of Thermokinematic Modeling Using PECUBE

Method, sample	Measured ages (Ma)	Modeled ages (Ma)	
		Slip rate constant = .45 km/My	One-step increase in slip rate
Zircon (U-Th)/He:			
12TYT5	12.5 ± 1.1	11.9	12.8
12TYT7	9.7 ± .7	9.9	9.7
Apatite fission track:			
12TYT5	9.2 ± 1.2	9.1	8.2
12TYT3	10.8 ± 1.7	8.2	6.9
12TYT7	7.8 ± 1.2	7.2	5.5
Apatite (U-Th)/He:			
12TYT5	4.9 ± .4	6.6	4.8
12TYT3	3.9 ± .2	5.9	3.9
12TYT7	3.0 ± .2	5.1	3.1

9.2 ± 1.2 Ma for this sample (12TYT5). Given that sample 12TYT3 (located in the middle of the profile) yielded an older AFT age of 10.8 ± 1.7 Ma (fig. 6) and that the uncertainties of the AFT ages are relatively large, we refrain from attempting a better fit of our model to the AFT data. Although two of the modeled AFT ages are younger than the measured ones, the mean fission-track length of 12.8 μm calculated from the best-fit model is in good agreement with the data (table 3). The PECUBE model with the temporally constant topography yields nearly identical results in terms of fault slip rate and onset of faulting (fig. A1, available online). However, the AHe ages of the model with evolving topography (i.e., 4.8 and 3.1 Ma for the topographically highest and lowest samples, respectively) are in better agreement with the measured AHe ages of 4.9 and 3.0 Ma than the AHe ages of the constant-topography model (i.e., 4.4 and 3.1 Ma; table 5). Therefore, we prefer the model with the evolving topography.

Discussion

U/Pb and Rb/Sr Ages. Our two U/Pb zircon ages of ~87 Ma for granite samples from the southern shore of Tangra Yumco are identical within error (fig. 4), and we interpret them to date the crystallization of a single granite intrusion in the footwall of the studied normal fault (fig. 3a, 3b). Such Late Cretaceous U/Pb ages for plutonic rocks in the northern Lhasa terrane have rarely been observed, although Haider et al. (2013) reported U/Pb ages of 85.5 ± 1.5 and 83.7 ± 1.1 Ma for a pluton near Lake Namco north of Lhasa. In general, granitoid intrusions in this region have

Early Cretaceous U/Pb ages between 140 and 100 Ma (Xu et al. 1985; Kapp et al. 2007; Hetzel et al. 2011; Haider et al. 2013).

The Rb/Sr ages on biotite for the three granite samples range from ~72 to ~60 Ma (fig. 5) and post-date the crystallization of the granitic intrusion by at least 15 My. As even large granitic intrusions cool from temperatures of 800°–700°C to ambient temperatures of the crust (300°–500°C) in less than a few million years (Jaeger 1964), the Rb/Sr ages cannot be related to the initially rapid cooling of the granite melt after its emplacement. Instead, we interpret the Rb/Sr ages to record slow cooling of the granite together with the surrounding crustal rocks through the closure temperature of biotite (i.e., ~350°C; Hunziker et al. 1992). This slow cooling was presumably the result of surface erosion and slow exhumation, because during the Late Cretaceous the Lhasa terrane experienced regional uplift and erosion (e.g., DeCelles et al. 2007), and there is no evidence for normal faulting at that time. If the thermal structure of the crust during this phase of slow cooling was not disturbed and if the spatial configuration of the samples has not changed, then the elevation dependence of the Rb/Sr biotite ages can be used to infer the rate of exhumation by erosion. Under these assumptions, the slope of the age-elevation relation (fig. 6) suggests an erosion rate of ~0.05 km/My during the latest Cretaceous and early Paleocene (i.e., just before the onset of the India-Asia collision). Although this interpretation is based on only three samples and should be corroborated with more data, it suggests that the cooling history of rocks from the footwalls of high-angle normal faults in Tibet may contain important information on processes much older than graben formation. In those parts of southern and central Tibet that were not affected by normal faulting, the rate of erosion after ~45 Ma decreased to low values of <0.05 km/My, as shown by thermochronological data (Hetzel et al. 2011; Rohrmann et al. 2012).

Thermokinematic Modeling of Thermochronological Data. Thermokinematic modeling of our AHe, AFT, and ZHe ages suggests that normal faulting at the Tangra Yumco graben began 14.5 ± 1.8 Ma (fig. 7). This age estimate is 2 My older than the oldest ZHe age of 12.5 ± 1.1 Ma, which provides only a minimum age for the initiation of faulting. The total fault slip rate in the best-fit model is 0.31 ± 0.02 km/My during the first stage of graben formation, whereas it is more than twice as high (i.e., 0.78 ± 0.05 km/My) during the second stage of faulting (table 6). The importance of accounting for heat advection in the fault footwall by thermokinematic modeling is illustrated by the difference between the apparent ex-

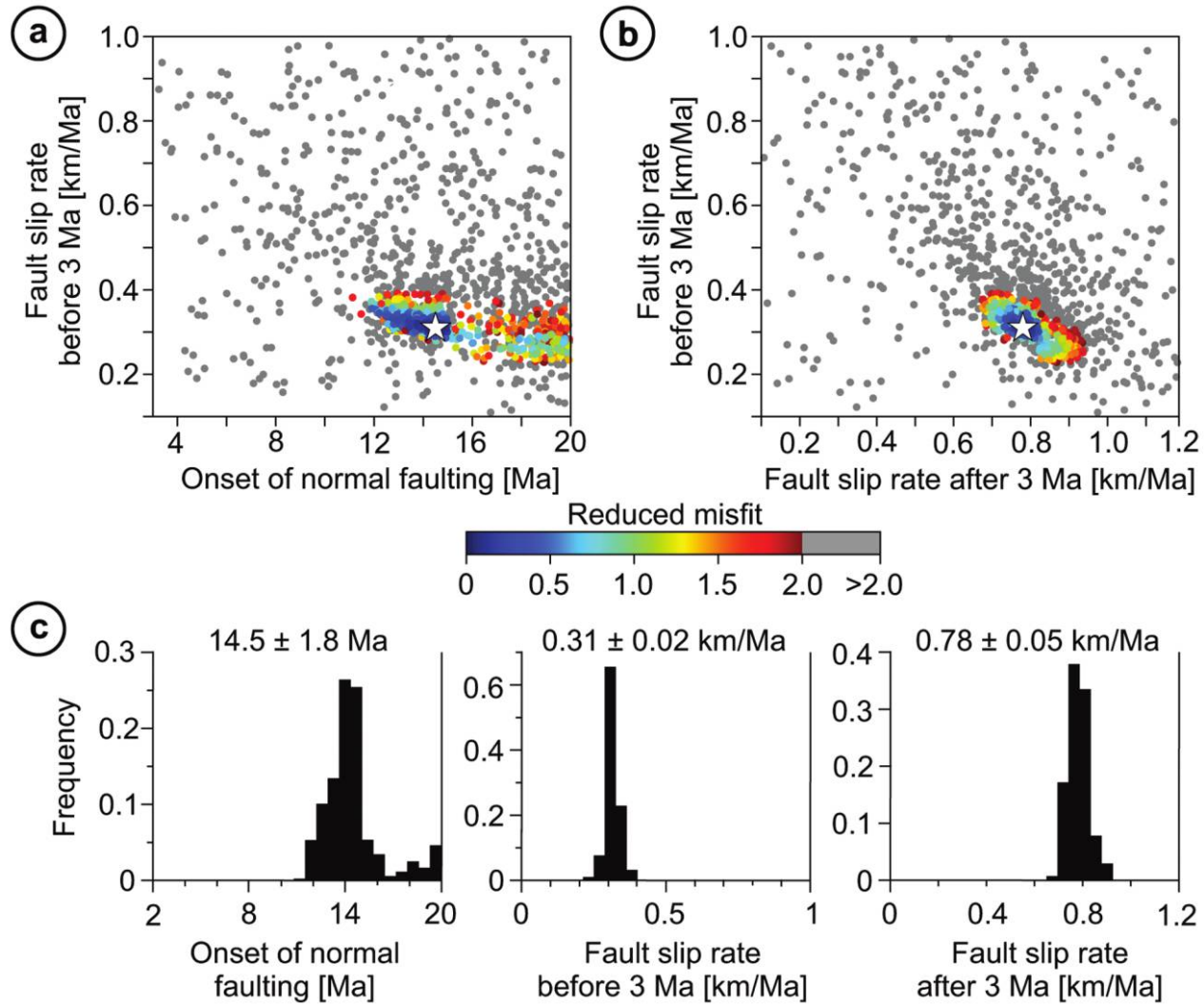


Figure 7. Results of the inversion procedure for 10,098 PECUBE models. Each dot corresponds to one model, and the star shows the best-fit model. *a, b*, Projection of all model results onto a plane defined by two of the three free model parameters (i.e., onset of faulting and fault slip rates before and after 3 Ma). The reduced misfit of the models was calculated following Braun et al. (2012). *c*, Mean values and standard deviations for three free model parameters based on marginal probability density functions.

humation rates, which are based on the age-elevation relations of the ZHe and AHe ages (i.e., ~ 0.20 and ~ 0.31 km/My; fig. 6), and the modeling results. Our best-fit model yields exhumation rates of 0.22 – 0.25 and 0.64 – 0.68 km/My (table 6), which are higher than the rates obtained from the age-elevation relationships, in particular during the second phase of faulting.

Although rates of normal faulting and exhumation in the model change instantaneously at 3 Ma, a more gradual increase seems more likely in nature. We speculate that the impact of glacial erosion in the study area may have increased in the late Pliocene, because the first major glaciations in the Northern Hemisphere occurred between ~ 2.8 and ~ 2.4 Ma (e.g., Maslin et al. 1998; Balco et al.

Table 6. Total Fault Slip, Slip Rates, Exhumation Rates, and Total Exhumation

Fault activity (Ma)	Total slip rate (km/My)	Vertical slip rate (km/My)	Exhumation rate (km/My)	Exhumation (km)
14.5–3.0	$.31 \pm .02$	$.28 \pm .02$	$.22$ – $.25$	2.5 – 2.9
3.0–0	$.78 \pm .05$	$.71 \pm .05$	$.64$ – $.68$	1.9 – 2.0

2005). We argue that the repeated growth of glaciers during the Quaternary ice ages has probably enabled a more efficient erosion of the rising footwall block (cf. Brozović et al. 1997; Egholm et al. 2009), as indicated by the deep U-shaped valleys (fig. 3a). With respect to enhanced erosion, it is noteworthy that three-dimensional numerical models coupling tectonics and surface processes predict an acceleration of slip on normal faults if the rate of footwall erosion increases (Maniatis et al. 2009). Hence, intensified glacial erosion may at least be partly responsible for the deduced increase in the rate of faulting.

Normal Faulting and Footwall Erosion. The total amount of exhumation during the two phases of faulting is 4.4–4.9 km in our thermokinematic model (table 6). Apart from high-angle normal faulting, erosion has also contributed to the exhumation of the mountain range south of Tangra Yumco, as shown by the presence of U-shaped valleys and the observation that the high peaks in the footwall are located about 5 km southwest of the fault trace (fig. 3b). The latter indicates that erosion was focused on the narrow mountain range in the fault footwall, which, in turn, may be related to a short wavelength of flexural uplift along the normal fault. As shown by Masek et al. (1994), the flexural uplift along Tibetan rifts is 1–2 km and spatially restricted to the narrow rift shoulders because the Tibetan upper crust has a low flexural rigidity of $2\text{--}6 \times 10^{20}$ N m, which is equivalent to an elastic thickness of only 4–6 km.

Published ^{10}Be concentrations of quartz from two stream-sediment samples (Rades et al. 2015; samples 12TYB4 and 12TYB11) can be used to estimate the current erosion rate in the mountain range south of Tangra Yumco, even though the calculation of such rates in glaciated regions is associated with considerable uncertainty (see Rades et al. 2015 for details). Using these ^{10}Be concentrations, we calculated spatially averaged ^{10}Be erosion rates of 260 ± 24 and 102 ± 9 mm/ky for the respective catchments (for locations, see fig. 2a) with version 2.3 of the CRONUS-Earth online calculator (Balco et al. 2008; <http://hess.ess.washington.edu>) and the time-independent scaling model of Lal (1991) and Stone (2000). As these erosion rates integrate over the past few thousand years only, they should be regarded as a rough estimate for the erosion of the mountain range during the Holocene. During Pleistocene glaciations the rate of erosion may have been higher. Given that our model suggests an exhumation rate of ~ 650 mm/ky (~ 0.65 km/My) during the past 3 My (table 6), it appears that, apart from normal faulting, erosion has contributed significantly to the exhumation of rocks in the fault footwall.

The pronounced erosion of the fault-bounded mountain range south of Tangra Yumco suggests that a significant volume of sediment has been generated during the formation of the Tangra Yumco graben. Hence, the southern lake basin of Tangra Yumco may contain a more or less continuous sedimentary record from the mid-Miocene to the present. Given that hitherto only late Quaternary lake sediments have been studied in the northern basin of Tangra Yumco (e.g., Long et al. 2015; Henkel et al. 2016), the lake may offer excellent opportunities for reconstructing past climate changes with long sediment cores.

Reasons for High-Angle versus Low-Angle Normal Faulting. The location of the Tangra Yumco rift coincides with a symmetry axis that is oriented subparallel to the India-Asia plate convergence vector and is defined by the diverging strike directions of normal faults (Kapp and Guynn 2004; fig. 8). Because of the arcuate shape of the Himalaya, the motion of India with respect to Asia becomes increasingly oblique when moving away from this symmetry axis and the region of purely normal India-Asia convergence (Seeber and Pêcher 1998; fig. 8). This, in turn, leads to an increased component of orogen-parallel extension along the Himalayan arc, which is documented by GPS data and the presence of kinematically linked normal and strike-slip faults (Styron et al. 2011 and references therein). The spatial distribution of rifts bounded by high-angle and low-angle normal faults provides further support for the oblique-convergence model of Styron et al. (2011), because graben systems bounded by high-angle normal faults occur predominantly in the region near the symmetry axis, where plate convergence is perpendicular to the Himalaya and arc-parallel extension is low (e.g., Tangra Yumco, Xainza, Thakkhola, Kung Co, Dinggye; fig. 8). In contrast, rifts with low-angle normal faults that record higher amounts of extension and experienced faster slip rates are located farther to the west and east, where the magnitude of arc-parallel extension is higher (e.g., Gurla Mandhata, Leo Pargil, Lunggar, Nyainqentanghla Shan) and the extensional structures are linked to strike-slip faults such as the right-lateral Karakorum fault (Murphy et al. 2002; Li and Yin 2008; fig. 8). For example, a high total displacement of more than ~ 35 km was estimated for the Gurla Mandhata detachment, and this detachment slipped at a high rate of 3–5 km/My during the major phase of extension (Murphy et al. 2002; McCallister et al. 2014). At the Lunggar rift, extension rates are high as well (i.e., ~ 1 to ~ 2.5 km/My), and the total amount of extension reaches ~ 10 to ~ 20 km, being variable along strike (Styron et al. 2013; Sundell et al. 2013). For most rifts

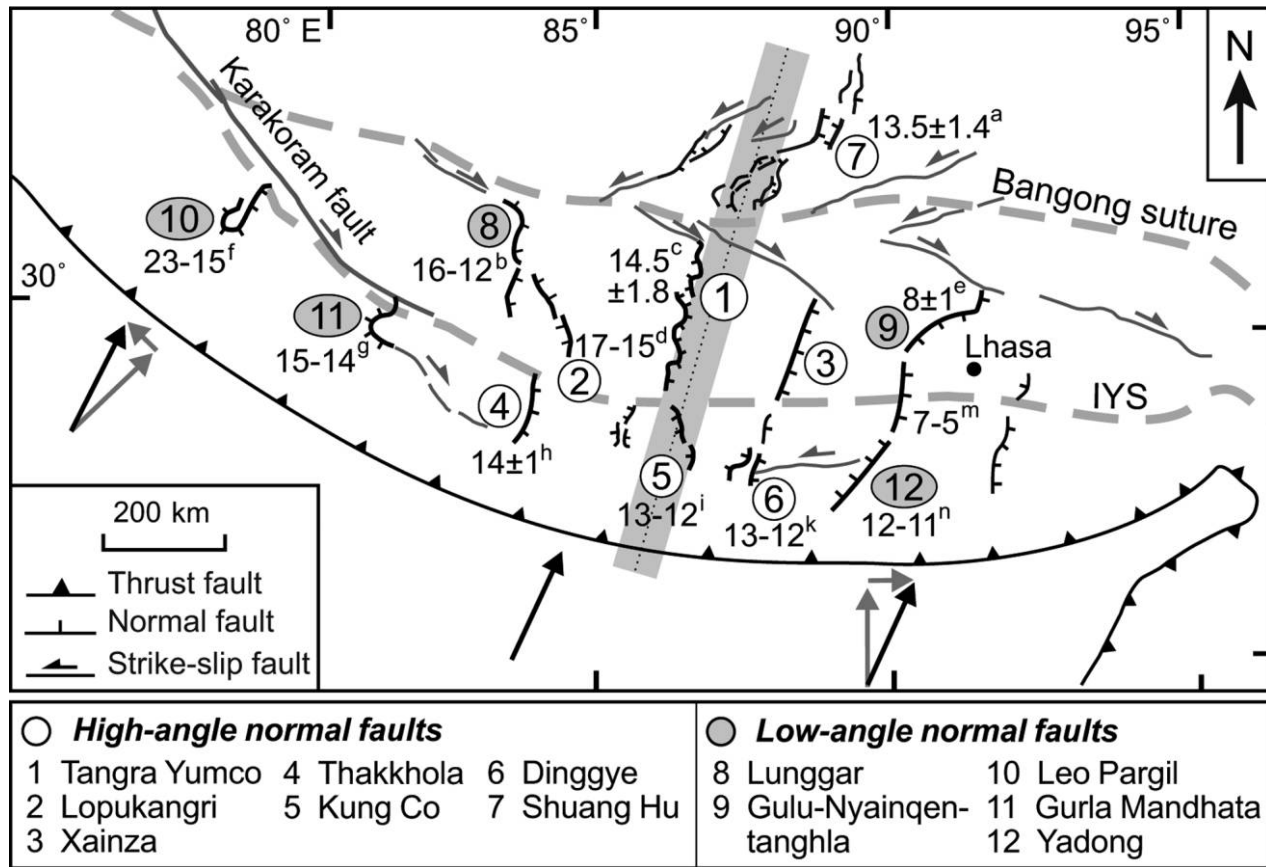


Figure 8. Major rifts in south-central Tibet and the Himalaya with initiation ages of normal faulting given in millions of years (Ma). Black arrows indicate the India-Asia convergence vector, whereas the arc-parallel and arc-orthogonal components are shown as gray arrows. The gray band indicates the symmetry axis of Kapp and Guynn (2004). Note that rifts with high-angle normal faults occur mainly near this symmetry axis, whereas low-angle normal faults are located farther west and east, where the arc-parallel component increases. The ages of individual rifts are based on age data from (a) Blisniuk et al. (2001), (b) Styron et al. (2013), (c) this study, (d) Laskowski et al. (2017), (e) Harrison et al. (1995) and Ratschbacher et al. (2011), (f) Thiede et al. (2006) and Langille et al. (2012), (g) McCallister et al. (2014), (h) Coleman and Hodges (1995), (i) Lee et al. (2011), (k) Kali et al. (2010), and (m, n) Ratschbacher et al. (2011). Suture zones are shown as dashed gray lines. IYS = Indus-Yarlung suture.

bounded by high-angle normal faults, slip rates and total amounts of extension are not well known yet, but it is likely that they are significantly lower than those for rifts with low-angle normal faults (cf. Friedman and Burbank 1995). At Tangra Yumco, fault slip rates determined in this study are <1 km/My (table 6). Farther to the north, at the Shuang Hu graben (fig. 8), an even lower slip rate of ~ 0.07 km/My was documented for the main graben-bounding fault (Blisniuk and Sharp 2003).

Regarding the timing of normal faulting in Tibet and the Himalaya, recent age compilations for the onset of faulting have shown that the beginning of extension is spatially variable (e.g., Ratschbacher et al. 2011; Sundell et al. 2013). Ages for the initiation of extension fall mainly in the range of ~ 15 – 10 Ma, but older and younger ages occur as well

(fig. 8). As a consequence, a single cause for the initiation of E-W extension in Tibet and the Himalaya, such as convective thinning or removal of the lithospheric mantle beneath much of Tibet during a narrow time interval (Molnar et al. 1993; Turner et al. 1993), appears to be unlikely. Whatever may be the ultimate reason(s) for extension, we argue that lateral temperature gradients (apart from the position relative to the symmetry axis discussed above) played an important role in controlling whether high-angle or low-angle normal faults formed during rifting. This is because the formation of low-angle normal faults and metamorphic core complexes requires a hot and low-viscosity middle to lower crust (e.g., Buck 1993; Tirel et al. 2008). High crustal temperatures allow ductile deformation at low shear stress and increase the strength contrast between the brittle

upper and ductile lower crust, thus favoring the formation of core complexes and detachment faults (Wijns et al. 2005; Wu et al. 2015; Labrousse et al. 2016). On the other hand, a low intracrustal strength contrast and a greater integrated lithospheric strength favor the formation of narrow rifts bounded by high-angle normal faults (Labrousse et al. 2016).

In the Lhasa and Qiangtang terranes, lateral temperature variations in the lower crust and upper mantle have been documented by the study of crustal and mantle xenoliths that occur in Oligocene to Pliocene volcanic rocks (Hacker et al. 2000; Ding et al. 2007; Chan et al. 2009). Lateral temperature variations are also indicated by shear-wave speed anomalies beneath south-central Tibet (e.g., Ceylan et al. 2012; Chen et al. 2017). Processes that may be responsible for such temperature variations include the tearing of the Indian slab (Ceylan et al. 2012) and/or the foundering of lower crust and mantle lithosphere (Chen et al. 2017) after crustal thickening during subduction and collision, as has been documented in the Pamir Mountains by petrological and geochronological studies of eclogite and granulite xenoliths (e.g., Ducea et al. 2003; Hacker et al. 2005; Gordon et al. 2012; Kooijman et al. 2017). Another factor that may have influenced both the structural style and the extension rate of rifts in Tibet is the underthrusting of cold Indian lithosphere beneath Tibet (Li et al. 2008; Nábělek et al. 2009; Ratschbacher et al. 2011; Sundell et al. 2013; Styron et al. 2015), which also ended the volcanism in southern Tibet (Chung et al. 2005; Liu et al. 2011).

Conclusions

Our new set of geochronological data constrains the cooling history of a granite body in the Lhasa terrane from its intrusion at mid-crustal depth to its exhumation at the surface. The granite intruded in

the Late Cretaceous at ~87 Ma, as shown by U/Pb zircon dating. After emplacement and initially rapid cooling, the granitic rocks experienced a long phase of slow cooling, which lasted at least until the early Paleocene and was presumably the result of slow erosion in this part of the Lhasa terrane. The younger episode of rifting and high-angle normal faulting at the Tangra Yumco graben began at ~15 Ma, as revealed by thermokinematic modeling of our low-temperature thermochronological data. Normal faulting and footwall exhumation proceeded at rates of about 0.2–0.3 km/My and accelerated to 0.6–0.8 km/My in the late Pliocene. The occurrence of both low-angle detachment and high-angle normal faults in Tibet and the Himalaya is presumably controlled by lateral temperature variations in the lower crust, which affect the strength ratio between upper and lower crust. A weak lower crust leads to a high intracrustal strength ratio and allows the formation of low-angle normal faults with large displacements. Conversely, a relatively strong lower crust causes the strength ratio to be low, which favors the generation of high-angle normal faults with limited displacement on individual faults.

ACKNOWLEDGMENTS

We are grateful to E. Rades and M. Strobl for providing the samples used in this study. We particularly thank C. Glotzbach for many discussions on PECUBE modeling. Sampling was performed during a field trip in 2012 that was related to the DFG (Deutsche Forschungsgemeinschaft [German Research Foundation]) priority program 1372 (grant HE 1704/11-1 to R. Hetzel). Comments by M. Tremblay, L. Ratschbacher, an anonymous reviewer, and the editor D. B. Rowley greatly improved the original manuscript.

REFERENCES CITED

- Armijo, R.; Tapponnier, P.; and Han, T. 1989. Late Cenozoic right-lateral strike-slip faulting in southern Tibet. *J. Geophys. Res.* 94(B3):2787–2838.
- Armijo, R.; Tapponnier, P.; Mercier, J. L.; and Han, T. L. 1986. Quaternary extension in southern Tibet. Field observations and tectonic implications. *J. Geophys. Res.* 91(B14):13,803–13,872.
- Balco, G.; Rovey, C. W., II; and Stone, J. O. 2005. The first glacial maximum in North America. *Science* 307:222.
- Balco, G.; Stone, J. O.; Lifton, N. A.; and Dunai, T. J. 2008. A complete and easily accessible means of calculation surface exposure ages or erosion rates from ^{10}Be and ^{26}Al measurements. *Quat. Geochronol.* 3:174–195.
- Blisniuk, P. M.; Hacker, B. R.; Glodny, J.; Ratschbacher, L.; Bi, S.; Wu, Z.; McWilliams, M. O.; and Calvert, A. 2001. Normal faulting in central Tibet since at least 13.5 Myr ago. *Nature* 412:628–632.
- Blisniuk, P. M., and Sharp, W. D. 2003. Rates of late Quaternary normal faulting in central Tibet from U-series dating of pedogenic carbonate in displaced fluvial gravel deposits. *Earth Planet. Sci. Lett.* 215:169–186.
- Braun, J. 2003. Pecube: a new finite-element code to solve the 3D heat transport equation including the effects of a time-varying, finite amplitude surface topography. *Comput. Geosci.* 29:787–794.

- Braun, J.; van der Beek, P.; Valla, P.; Robert, X.; Herman, F.; Glotzbach, C.; Pedersen, V.; Perry, C.; Simon-Labric, T.; and Prigent, C. 2012. Quantifying rates of landscape evolution and tectonic processes by thermochronology and numerical modeling of crustal heat transport using PECUBE. *Tectonophysics* 524–525:1–28.
- Brozović, N.; Burbank, D. W.; and Meigs, A. J. 1997. Climatic limits on landscape development in the northwestern Himalaya. *Science* 276:571–574.
- Buck, W. R. 1993. Effect of lithospheric thickness on the formation of high- and low-angle normal faults. *Geology* 21:933–936.
- Burtner, R. L.; Nigrini, A.; and Donelick, R. A. 1994. Thermochronology of Lower Cretaceous source rocks in the Idaho-Wyoming thrust belt. *Am. Assoc. Pet. Geol. Bull.* 78:1613–1636.
- Campani, M.; Herman, F.; and Mancktelow, N. 2010. Two- and three-dimensional thermal modeling of a low-angle detachment: exhumation history of the Simplon Fault Zone, central Alps. *J. Geophys. Res.* 115: B10420. doi:10.1029/2009JB007036.
- Ceylan, S.; Ni, J.; Chen, J. Y.; Zhang, Q.; Tilmann, F.; and Sandvol, E. 2012. Fragmented Indian plate and vertically coherent deformation beneath eastern Tibet. *J. Geophys. Res.* 117: B11303. doi:10.1029/2012JB009210.
- Chan, G. H.-N.; Waters, D. J.; Searle, M. P.; Aitchison, J. C.; Horstwood, M. S. A.; Crowley, Q.; Lo, C.-H.; and Chan, J. S.-L. 2009. Probing the basement of southern Tibet: evidence from crustal xenoliths entrained in a Miocene ultrapotassic dyke. *J. Geol. Soc. Lond.* 166: 45–52.
- Chen, M.; Niu, F.; Tromp, J.; Lenardic, A.; Lee, C.-T. A.; Cao, W.; and Ribeiro, J. 2017. Lithospheric foundering and underthrusting imaged beneath Tibet. *Nat. Commun.* 8:15659. doi:10.1038/ncomms15659.
- Chung, S.-L.; Chu, M.-F.; Zhang, Y.; Xie, Y.; Lo, C.-H.; Lee, T.-Y.; Lan, C.-Y.; Li, X.; Zhang, Q.; and Wang, Y. 2005. Tibetan tectonic evolution inferred from spatial and temporal variations in post-collisional magmatism. *Earth Sci. Rev.* 68:173–196.
- Coleman, M., and Hodges, K. 1995. Evidence for Tibetan plateau uplift before 14 Myr ago from a new minimum age for east-west extension. *Nature* 374:49–52.
- DeCelles, P. G.; Kapp, P.; Ding, L.; and Gehrels, G. E. 2007. Late Cretaceous to middle Tertiary basin evolution in the central Tibetan Plateau: changing environments in response to tectonic partitioning, aridification, and regional elevation gain. *Geol. Soc. Am. Bull.* 119:654–680.
- DeCelles, P. G.; Kapp, P.; Gehrels, G. E.; and Ding, L. 2014. Paleocene-Eocene foreland basin evolution in the Himalaya of southern Tibet and Nepal: implications for the age of initial India-Asia collision. *Tectonics* 33:824–849.
- Dewane, T. J.; Stockli, D. F.; Hager, C.; Taylor, M.; Ding, L.; Lee, J.; and Wallis, S. 2006. Timing of Cenozoic E-W extension in the Tangra Yum Co-Kung Co rift, south-central Tibet. *American Geophysical Union Fall Meeting (San Francisco, 2006)*, abstract T34C-04.
- Ding, L.; Kapp, P.; Yahui, Y.; and Lai, Q. 2007. Postcollisional calc-alkaline lavas and xenoliths from the southern Qiangtang terrane, central Tibet. *Earth Planet. Sci. Lett.* 254:28–38.
- Donelick, R. A.; Ketcham, R. A.; and Carlson, W. D. 1999. Variability of apatite fission-track annealing kinetics: II. Crystallographic orientation effects. *Am. Mineral.* 84:1224–1234.
- Ducea, M.; Lutkov, V.; Minaev, V.; Hacker, B. R.; Ratschbacher, L.; Luffi, P.; Schwab, M.; et al. 2003. Building the Pamirs: the view from the underside. *Geology* 31: 849–852.
- Dumitru, T. A. 1993. A new computer-automated microscope stage system for fission-track analysis. *Nucl. Tracks Radiat. Meas.* 21:575–580.
- Dunkl, I. 2002. Trackkey: a Windows program for calculation and graphical presentation of fission track data. *Comput. Geosci.* 28:3–12.
- Dunkl, I.; Grasemann, B.; and Frisch, W. 1998. Thermal effects of exhumation of a metamorphic core complex on hanging wall syn-rift sediments: an example from the Rechnitz Window, eastern Alps. *Tectonophysics* 297:31–50.
- Dunkl, I.; Mikes, T.; Simon, K.; and von Eynatten, H. 2008. Brief introduction to the Windows program Pepita: data visualization, and reduction, outlier rejection, calculation of trace element ratios and concentrations from LA-ICP-MS data. *In* Sylvester, P., ed. *Laser ablation ICP-MS in the earth sciences: current practices and outstanding issues*. Mineral. Assoc. Can. Short Course 40:334–340.
- Egholm, D. L.; Nielsen, S. B.; Pedersen, V. K.; and Lese-mann, J. E. 2009. Glacial effects limiting mountain height. *Nature* 460:884–887.
- Ehlers, T. A. 2005. Crustal thermal processes and the interpretation of thermochronometer data. *In* Reiners, P. W., and Ehlers, T. A., eds. *Low-temperature thermochronology: techniques, interpretations, and applications*. *Rev. Mineral. Geochem.* 58:315–350.
- Ehlers, T. A.; Armstrong, P. A.; and Chapman, D. S. 2001. Normal fault thermal regimes and the interpretation of low-temperature thermochronometers. *Phys. Earth Planet. Inter.* 126:179–194.
- Farley, K. A. 2000. Helium diffusion from apatite: general behavior as illustrated by Durango fluorapatite. *J. Geophys. Res.* 105(B2):2903–2914.
- Farley, K. A.; Wolf, R. A.; and Silver, L. T. 1996. The effects of long alpha-stopping distances on (U-Th)/He ages. *Geochim. Cosmochim. Acta* 60:4223–4229.
- Flowers, R. M.; Ketcham, R. A.; Shuster, D. L.; and Farley, K. A. 2009. Apatite (U-Th)/He thermochronometry using a radiation damage accumulation and annealing model. *Geochim. Cosmochim. Acta* 73:2347–2365.
- Forsyth, D. W. 1992. Finite extension and low-angle normal faulting. *Geology* 20:27–30.
- Frei, D., and Gerdes, A. 2009. Precise and accurate in situ U-Pb dating of zircon with high sample throughput by automated LA-SF-ICP-MS. *Chem. Geol.* 261:261–270.

- Friedmann, S. J., and Burbank, D. W. 1995. Rift basins and supradetachment basins: intracontinental extensional end-members. *Basin Res.* 7:109–127.
- Galbraith, R. F., and Laslett, G. M. 1993. Statistical models for mixed fission-track ages. *Nucl. Tracks Radiat. Meas.* 21:459–470.
- Garzzone, C. N.; DeCelles, P. G.; Hodkinson, D. G.; Ojha, T. P.; and Upreti, B. N. 2003. East-west extension and Miocene environmental change in the southern Tibetan Plateau: Thakkhola graben, central Nepal. *Geol. Soc. Am. Bull.* 115:3–20.
- Gautheron, C.; Tassan-Got, L.; Barbarand, J.; and Pagel, M. 2009. Effect of alpha-damage annealing on apatite (U-Th)/He thermochronology. *Chem. Geol.* 266:157–170.
- Geological Survey of Jiangxi Province. 2002. Geological maps of the Bangduo and Cuomai districts (scale: 1:250,000).
- Gleadow, A. J. W. 1981. Fission-track dating methods: what are the real alternatives? *Nucl. Tracks* 5:3–14.
- Glotzbach, C.; van der Beek, P. A.; and Spiegel, C. 2011. Episodic exhumation and relief growth in the Mont Blanc massif, Western Alps from numerical modelling of thermochronology data. *Earth Planet. Sci. Lett.* 304:417–430.
- Gordon, S. M.; Luffi, P.; Hacker, B.; Valley, J.; Spicuzza, M.; Kozdon, R.; Kelemen, P.; Ratschbacher, L.; and Minaev, V. 2012. The thermal structure of continental crust in active orogens: insight from Miocene eclogite and granulite xenoliths of the Pamir Mountains. *J. Metamorph. Geol.* 30:413–434.
- Grasemann, B., and Dunkl, I. 2003. Effects of the geometry of normal faulting on the near surface heat flow during extension: the example of the Rechnitz Metamorphic Core Complex (Austria). *Mitt. Oesterr. Geol. Ges.* 93:87–103.
- Green, P. F. 1981. A new look at statistics in fission-track dating. *Nucl. Tracks* 5:77–86.
- Guenther, W. R.; Reiners, P. W.; Ketcham, R. A.; Nasdala, L.; and Giester, G. 2013. Helium diffusion in natural zircon: radiation damage, anisotropy, and the interpretation of zircon (U-Th)/He thermochronology. *Am. J. Sci.* 313:145–198.
- Hacker, B.; Luffi, P.; Lutkov, V.; Minaev, V.; Ratschbacher, L.; Plank, T.; Ducea, M.; Patiño-Douce, A.; McWilliams, M.; and Metcalf, J. 2005. Near-ultrahigh pressure processing of continental crust: Miocene crustal xenoliths from the Pamir. *J. Petrol.* 46:1661–1687.
- Hacker, B. R.; Gnos, E.; Ratschbacher, L.; Grove, M.; McWilliams, M.; Sobolev, S. V.; Wan, J.; and Wu, Z. 2000. Hot and dry deep crustal xenoliths from Tibet. *Science* 287:2463–2466.
- Haider, V. L.; Dunkl, I.; von Eynatten, H.; Ding, L.; Frei, D.; and Zhang, L. 2013. Cretaceous to Cenozoic evolution of the northern Lhasa Terrane and the Early Paleogene development of peniplains at Nam Co, Tibetan Plateau. *J. Asian Earth Sci.* 70–71:79–98.
- Harrison, T. M.; Copeland, P.; Kidd, W. S. F.; and Lovera, O. M. 1995. Activation of the Nyainqentanghla Shear Zone: implications for uplift of the southern Tibetan Plateau. *Tectonics* 14:658–676.
- Harrison, T. M.; Copeland, P.; Kidd, W. S. F.; and Yin, A. 1992. Raising Tibet. *Science* 255:1663–1670.
- Henkel, K.; Haberzettl, T.; St-Onge, G.; Wang, J.; Ahlborn, M.; Daut, G.; Zhu, L.; and Mäusbacher, R. 2016. High-resolution paleomagnetic and sedimentological investigations on the Tibetan Plateau for the past 16 ka cal B.P.—the Tangra Yumco record. *Geochem. Geophys. Geosyst.* 17:774–790.
- Hetzl, R.; Dunkl, I.; Haider, V.; Strobl, M.; von Eynatten, H.; Ding, L.; and Frei, D. 2011. Peniplain formation in southern Tibet predates the India-Asia collision and plateau uplift. *Geology* 39:983–986.
- Hourigan, J.; Reiners, P. W.; and Brandon, M. T. 2005. U-Th zonation-dependent alpha-ejection in (U-Th)/He chronometry. *Geochim. Cosmochim. Acta* 69:3349–3365.
- Hunziker, J. C.; Desmons, J.; and Hurford, A. J. 1992. Thirty-two years of geochronological work in the Central and Western Alps: a review on seven maps. *Mem. Geol. Lausanne* 13.
- Hurford, A. J. 1998. Zeta: the ultimate solution to fission-track analysis calibration or just an interim measure. *In* van den Haute, P., and De Corte, F., eds. *Advances in fission-track geochronology*. *Solid Earth Sci. Lib.* 10. Dordrecht, Kluwer, p. 19–32.
- Hurford, A. J., and Green, P. F. 1983. The zeta age calibration of fission-track dating. *Chem. Geol.* 41:285–317.
- Jackson, S.; Pearson, N.; Griffin, W.; and Belousova, E. 2004. The application of laser ablation-inductively coupled plasma-mass spectrometry to in situ U-Pb zircon geochronology. *Chem. Geol.* 211:47–69.
- Jaeger, J. C. 1964. Thermal effects of intrusions. *Rev. Geophys.* 2:443–466.
- Jessup, M. J.; Newell, D. L.; Cottle, J. M.; Berger, A. L.; and Spotila, J. A. 2008. Orogen-parallel extension and exhumation enhanced by denudation in the trans-Himalayan Arun River gorge, Ama Drime Massif, Tibet-Nepal. *Geology* 36:587–590.
- Kali, E.; Leloup, P. H.; Arnaud, N.; Mahéo, G.; Liu, D.; Boutonnet, E.; van der Woerd, J.; Liu, X.; Jing, L.-Z.; and Li, H. 2010. Exhumation history of the deepest central Himalayan rocks, Ama Drime range: key pressure-temperature-deformation-time constraints on orogenic models. *Tectonics* 29:TC2014. doi:10.1029/2009TC002551.
- Kapp, J. L. D.; Harrison, T. M.; Kapp, P.; Grove, M.; Lovera, O. M.; and Ding, L. 2005. Nyainqentanghla Shan: a window into the tectonic, thermal, and geochemical evolution of the Lhasa block, southern Tibet. *J. Geophys. Res.* 110:B08413. doi:10.1029/2004JB003330.
- Kapp, P.; DeCelles, P. G.; Gehrels, G. E.; Heizler, M.; and Ding, L. 2007. Geological records of the Lhasa-Qiangtang and Indo-Asian collisions in the Nima area of central Tibet. *Geol. Soc. Am. Bull.* 119:917–933.
- Kapp, P., and Guynn, J. H. 2004. Indian punch rifts Tibet. *Geology* 32:993–996.

- Kapp, P.; Taylor, M.; Stockli, D.; and Ding, L. 2008. Development of active low-angle normal fault systems during orogenic collapse: insight from Tibet. *Geology* 36:7–10.
- Ketchum, R. A. 2005. Forward and inverse modeling of low-temperature thermochronometry data. *In* Reiners, P. W., and Ehlers, T. A., eds. *Low-temperature thermochronology: techniques, interpretations, and applications*. *Rev. Mineral. Geochem.* 58:275–314.
- Kooijman, E.; Smit, M. A.; Ratschbacher, L.; and Kylander-Clark, A. R. C. 2017. A view into crustal evolution at mantle depths. *Earth Planet. Sci. Lett.* 465:59–69.
- Labrousse, L.; Huet, B.; Le Pourhiet, L.; Jolivet, L.; and Burov, E. 2016. Rheological implications of extensional detachments: Mediterranean and numerical insights. *Earth Sci. Rev.* 161:233–258.
- Lal, D. 1991. Cosmic ray labeling of denudation surfaces: in situ nuclide production rates and denudation models. *Earth Planet. Sci. Lett.* 104:424–439.
- Langille, J. M.; Jessup, M. J.; Cottle, J. M.; Lederer, G.; and Ahmad, T. 2012. Timing of metamorphism, melting and exhumation of the Leo Pargil dome, northwest India. *J. Metamorph. Geol.* 30:769–791.
- Laskowski, A. K.; Kapp, P.; Ding, L.; Campbell, C.; and Liu, X. 2017. Tectonic evolution of the Yarlung suture zone, Lopa Range region, southern Tibet. *Tectonics* 36:108–136.
- Lee, J.; Hager, C.; Wallis, S. R.; Stockli, D. F.; Whitehouse, M. J.; Aoya, M.; and Wang, Y. 2011. Middle to late Miocene extremely rapid exhumation and thermal reequilibration in the Kung Co rift, southern Tibet. *Tectonics* 30:TC2007. doi:10.1029/2010TC002745.
- Li, C.; van der Hilst, R. D.; Meltzer, A. S.; and Engdahl, E. R. 2008. Subduction of the Indian lithosphere beneath the Tibetan Plateau and Burma. *Earth Planet. Sci. Lett.* 274:157–168.
- Li, D., and Yin, A. 2008. Orogen-parallel, active left-slip faults in the eastern Himalaya: implications for the growth mechanism of the Himalayan Arc. *Earth Planet. Sci. Lett.* 274:258–267.
- Liu, C. Z.; Wu, F. Y.; Chung, S. L.; and Zhao, Z. D. 2011. Fragments of hot and metasomatized mantle lithosphere in middle Miocene ultrapotassic lavas, southern Tibet. *Geology* 39:923–926.
- Long, H.; Haberzettl, T.; Tsukamoto, S.; Shen, J.; Kasper, T.; Daut, G.; Zhu, L.; Mäusbacher, R.; and Frechen, M. 2015. Luminescence dating of lacustrine sediments from Tangra Yumco (southern Tibetan Plateau) using post-IR IRSL signals from polymineral grains. *Boreas* 44:139–152.
- Ludwig, K. R. 2012. User's manual for ISOPLOT/Ex 3.41c: a geochronological toolkit for Microsoft Excel. Spec. Publ. 4. Berkeley, CA, Berkeley Geochronology Center, 70 p.
- Mahéo, G.; Leloup, P. H.; Valli, F.; Lacassin, R.; Arnaud, N.; Paquette, J.-L.; Fernandez, A.; Haibling, L.; Farley, K. A.; and Tapponnier, P. 2007. Post 4 Ma initiation of normal faulting in southern Tibet. Constraints from the Kung Co half graben. *Earth Planet. Sci. Lett.* 256:233–243.
- Mancktelow, N. S., and Grasemann, B. 1997. Time-dependent effects of heat advection and topography on cooling histories during erosion. *Tectonophysics* 270:167–195.
- Maniatis, G.; Kurfeß, D.; Hampel, A.; and Heidbach, O. 2009. Slip acceleration on normal faults due to erosion and sedimentation—results from a new three-dimensional numerical model coupling tectonics and landscape evolution. *Earth Planet. Sci. Lett.* 284:570–582.
- Marillo-Sialer, E.; Woodhead, J.; Hergt, J.; Greig, A.; Guillong, M.; Gleadow, A.; Evans, N.; and Paton, C. 2014. The zircon 'matrix effect': evidence for an ablation rate control on the accuracy of U-Pb age determinations by LA-ICP-MS. *J. Anal. Atom. Spectrom.* 29:981–989.
- Masek, J. G.; Isacks, B. L.; Fielding, E. J.; and Browaeys, J. 1994. Rift flank uplift in Tibet: evidence for a viscous lower crust. *Tectonics* 13:659–667.
- Maslin, M. A.; Li, X. S.; Loutre, M.-F.; and Berger, A. 1998. The contribution of orbital forcing to the progressive intensification of Northern Hemisphere glaciation. *Quat. Sci. Rev.* 17:411–426.
- McCallister, A. T.; Taylor, M. H.; Murphy, M. A.; Styron, R. H.; and Stockli, D. F. 2014. Thermochronologic constraints on the late Cenozoic exhumation history of the Gurla Mandhata metamorphic core complex, southwestern Tibet. *Tectonics* 33:27–52.
- Molnar, P.; England, P.; and Martinod, J. 1993. Mantle dynamics, uplift of the Tibetan Plateau, and the Indian Monsoon. *Rev. Geophys.* 31:357–396.
- Molnar, P., and Tapponnier, P. 1975. Cenozoic tectonics of Asia: effects of a continental collision. *Science* 189:419–426.
- . 1978. Active tectonics of Tibet. *J. Geophys. Res.* 83(B11):5361–5375.
- Murphy, M. A.; Sanchez, V.; and Taylor, M. H. 2010. Syncollisional extension along the India-Asia suture zone, south-central Tibet: implications for crustal deformation of Tibet. *Earth Planet. Sci. Lett.* 290:233–243.
- Murphy, M. A.; Yin, A.; Kapp, P.; Harrison, T. M.; Manning, C. E.; Ryerson, F. J.; Ding, L.; and Guo, J. 2002. Structural evolution of the Gurla Mandhata detachment system, southwest Tibet: implications for the eastward extent of the Karakoram fault system. *Geol. Soc. Am. Bull.* 114:428–447.
- Nábělek, J.; Hetényi, G.; Vergne, J.; Sapkota, S.; Kafle, B.; Jiang, M.; Su, H.; Chen, J.; Huang, B. S.; and Hi-CLIMB Team. 2009. Underplating in the Himalaya-Tibet collision zone revealed by the Hi-CLIMB experiment. *Science* 325:1371–1374.
- Rades, E. F.; Hetzel, R.; Strobl, M.; Xu, Q.; and Ding, L. 2015. Defining rates of landscape evolution in a south Tibetan graben with *in situ*-produced cosmogenic ¹⁰Be. *Earth Surf. Proc. Landforms* 40:1862–1876.
- Ratschbacher, L.; Krumrei, I.; Blumenwitz, M.; Staiger, M.; Gloaguen, R.; Miller, B. V.; Samson, S. D.; Edwards, M. A.; and Appel, E. 2011. Rifting and strike-slip shear

- in central Tibet and the geometry, age and kinematics of upper crustal extension in Tibet. *In* Gloaguen, R., and Ratschbacher, L., eds. Growth and collapse of the Tibetan Plateau. *Geol. Soc. Lond. Spec. Publ.* 353:127–163.
- Reiners, P. W. 2005. Zircon (U-Th)/He thermochronometry. *In* Reiners, P. W., and Ehlers, T. A., eds. Low-temperature thermochronology: techniques, interpretations, and applications. *Rev. Mineral. Geochem.* 58:151–179.
- Reiners, P. W., and T. A. Ehlers, eds. 2005. Low-temperature thermochronology: techniques, interpretations, and applications. *Rev. Mineral. Geochem.* 58.
- Reiners, P. W.; Spell, T. L.; Nicolescu, S.; and Zanetti, K. A. 2004. Zircon (U-Th)/He thermochronometry: He diffusion and comparisons with $^{10}\text{Ar}/^{39}\text{Ar}$ dating. *Geochim. Cosmochim. Acta* 68:1857–1887.
- Rohrman, A.; Kapp, P.; Carrapa, B.; Reiners, P. W.; Gynn, J.; Ding, L.; and Heizler, M. 2012. Thermochronologic evidence for plateau formation in central Tibet by 45 Ma. *Geology* 40:187–190.
- Rowley, D. B. 1996. Age of initiation of collision between India and Asia: a review of stratigraphic data. *Earth Planet. Sci. Lett.* 145:1–13.
- Sambridge, M. 1999a. Geophysical inversion with a neighbourhood algorithm—I. Searching a parameter space. *Geophys. J. Int.* 138:479–494.
- . 1999b. Geophysical inversion with a neighbourhood algorithm—II. Appraising the ensemble. *Geophys. J. Int.* 138:727–746.
- Sanchez, V. I.; Murphy, M. A.; Robinson, A. C.; Lapen, T. J.; and Heizler, M. T. 2013. Tectonic evolution of the India-Asia suture zone since middle Eocene time, Lopukangri area, south-central Tibet. *J. Asian Earth Sci.* 62:205–220.
- Seeber, L., and Pêcher, A. 1998. Strain partitioning along the Himalayan arc and the Nanga Parbat antiform. *Geology* 26:791–794.
- Sláma, J.; Košler, J.; Condon, D. J.; Crowley, J. L.; Gerdes, A.; Hanchar, J. M.; Horstwood, M. S. A.; et al. 2008. Plešovice zircon—a new natural reference material for U-Pb and Hf isotopic microanalysis. *Chem. Geol.* 249:1–35.
- Sliwinski, J. T.; Guillong, M.; Liebske, C.; Dunkl, I.; von Quadt, A.; and Bachmann, O. 2017. Improved accuracy of LA-ICP-MS U-Pb ages of Cenozoic zircons by alpha dose correction. *Chem. Geol.* 472:8–21.
- Stockli, D. F. 2005. Application of low-temperature thermochronometry to extensional tectonic settings. *In* Reiners, P. W., and Ehlers, T. A., eds. Low-temperature thermochronology: techniques, interpretations, and applications. *Rev. Mineral. Geochem.* 58:411–448.
- Stone, J. O. 2000. Air pressure and cosmogenic isotope production. *J. Geophys. Res.* 105(B10):23,753–23,759.
- Stüwe, K.; White, L.; and Brown, R. 1994. The influence of eroding topography on steady-state isotherms. Application to fission track analysis. *Earth Planet. Sci. Lett.* 124:63–74.
- Styron, R.; Taylor, M.; and Murphy, M. A. 2011. Oblique convergence, arc-parallel extension, and the role of strike-slip faulting in the High Himalaya. *Geosphere* 7:582–596.
- Styron, R.; Taylor, M.; and Sundell, K. 2015. Accelerated extension of Tibet linked to the northward underthrusting of Indian crust. *Nat. Geosci.* 8:131–134.
- Styron, R.; Taylor, M.; Sundell, K.; Stockli, D. F.; Oalman, J. A. G.; Möller, A.; McCallister, A. T.; Liu, D.; and Ding, L. 2013. Miocene initiation and acceleration of extension in the South Lunggar rift, western Tibet: evolution of an active detachment system from structural mapping and (U-Th)/He thermochronology. *Tectonics* 32:880–907.
- Sundell, K. E.; Taylor, M. H.; Styron, R. H.; Stockli, D. F.; Kapp, P.; Hager, C.; Liu, D.; and Ding, L. 2013. Evidence for constriction and Pliocene acceleration of east-west extension in the North Lunggar rift region of west central Tibet. *Tectonics* 32:1454–1479.
- Taylor, M.; Yin, A.; Ryerson, F. J.; Kapp, P.; and Ding, L. 2003. Conjugate strike-slip faulting along the Bangong-Nujiang suture zone accommodates coeval east-west extension and north-south shortening in the interior of the Tibetan Plateau. *Tectonics* 22:1044. doi:10.1029/2002TC001361.
- Thiede, R. C.; Arrowsmith, J. R.; Bookhagen, B.; McWilliams, M.; Sobel, E. R.; and Strecker, M. R. 2006. Dome formation and extension in the Tethyan Himalaya, Leo Pargil, northwest India. *Geol. Soc. Am. Bull.* 118: 635–650.
- Tirel, C.; Brun, J.-P.; and Burov, E. 2008. Dynamics and structural development of metamorphic core complexes. *J. Geophys. Res.* 113:B04403. doi:10.1029/2005JB003694.
- Turner, S.; Hawkesworth, C.; Liu, J.; Rogers, N.; Kelley, S.; and van Calsteren, P. 1993. Timing of Tibetan uplift constrained by analysis of volcanic rocks. *Nature* 364:50–54.
- Villa, I. M.; de Bièvre, P.; Holden, N. E.; and Renne, P. R. 2015. IUPAC-IUGS recommendation on the half life of ^{87}Rb . *Geochim. Cosmochim. Acta* 164:382–385.
- Wagner, G. A., and Reimer, G. M. 1972. Fission track tectonics: the tectonic interpretation of fission track apatite ages. *Earth Planet. Sci. Lett.* 14:263–268.
- Wiedenbeck, M.; Allé, P.; Corfu, F.; Griffin, W. L.; Meier, M.; Oberli, F.; von Quadt, A.; Roddick, J. C.; and Spiegel, W. 1995. Three natural zircon standards for U-Th-Pb, Lu-Hf, trace element and REE analyses. *Geostandard. Newslett.* 19:1–23.
- Wijns, C.; Weinberg, R.; Gessner, K.; and Moresi, L. 2005. Mode of crustal extension determined by rheological layering. *Earth Planet. Sci. Lett.* 236:120–134.
- Wolff, R.; Dunkl, I.; Kiesselbach, G.; Wemmer, K.; and Siegesmund, S. 2012. Thermochronological constraints on the multiphase exhumation history of the Ivrea-Verbano zone of the Southern Alps. *Tectonophysics* 579:104–117.
- Wu, G.; Lavie, L. L.; and Choi, E. 2015. Modes of continental extension in a crustal wedge. *Earth Planet. Sci. Lett.* 421:89–97.

- Xu, R.-H.; Schärer, U.; and Allègre, C. J. 1985. Magmatism and metamorphism in the Lhasa Block (Tibet): a geochronological study. *J. Geol.* 93:41–57.
- Yin, A., and Harrison, T. M. 2000. Geologic evolution of the Himalayan-Tibetan orogen. *Annu. Rev. Earth Planet. Sci.* 28:211–280.
- Zaun, P., and Wagner, G. A. 1985. Fission track stability in zircon under geological conditions. *Nucl. Tracks Radiat. Meas.* 10:303–307.
- Zhang, Q.; Willems, H.; Ding, L.; Gräfe, K.-U.; and Appel, E. 2012. Initial India-Asia continental collision and foreland basin evolution in the Tethyan Himalaya of Tibet: evidence from stratigraphy and paleontology. *J. Geol.* 120:175–189.
- Zhu, B.; Kidd, W. S. F.; Rowley, D. B.; Currie, B. S.; and Shafique, N. 2005. Age of initiation of the India-Asia collision in the east-central Himalaya. *J. Geol.* 113:265–285.